#### **UNIVERSITY OF RELIZANE**

#### Faculty of Science and Technology Department of Physics



#### **Doctoral Thesis LMD 3éme Cycle**

**Branch:** Physics

**Speciality:** Physics of Materials

**Presented by** 

Mr. CHEFA Abdelbasat

#### Thesis title:

'Ab-initio study of ternary intermetallic alloys based on substituted magnetic or nonmagnetic elements.'

#### In front of a jury composed of:

President	FARES Redouane	MCA	University of Relizane
Thesis Director	BERRAHAL Mokhtar	MCA	Higher Normal School of Oran -ENSO -AMMOUR Ahmed
Assistant Thesis Director	MIR Ali	Pr	University of Relizane
Examiner	MESBAH Smain	MCA	University of Relizane
Examiner	MOULAY Noureddine	Pr	University of Sidi Bel Abbas

University year 2024-2025

### **Dedication**

To my beloved parents, your love, sacrifices, and unwavering support have been my greatest strength. Every step I've taken is thanks to your guidance and care. To my dear brothers and sisters, Your encouragement and presence have always lifted me higher. Thank you for being my constant source of inspiration.

To my teachers thank for your guides and thank you for being my constant source of inspiration.

Abdelbasat Chefa

## Appreciation

First and foremost, i thank Allah, almighty, for giving me the strength to survive, and praise for overcoming all the difficulties

I would like to thank Dr. **BERRHAL MOKHTAR** of AMMOUR Ahmed Normale Superior School of Oran, and **Mir ALI** Professor at the University of Relizane, who supervised me throughout this thesis and shared his brilliant insights with me. I would also like to thank him for his kindness and constant availability, and for the many words of encouragement he gave me.

I would like to thank the committee that will review this thesis and thank you for your efforts.

Finaly, I would like to thank Ms. Ouflla for her moral support during my journey to complete my academic career and thank my honorable professors and everyone who taught me and guided me during my journey as a student. And big thanks for university of Relizane and their Officials

#### **Abstract**

In this thesis, Density Functional Theory (DFT) within the LSDA framework, implemented in WIEN2k, was used to explore the structural, magnetic, electronic, elastic and thermoelectric properties of the intermetallic compound DyFe<sub>3</sub>Ni<sub>12</sub>. A comparison of different arrangements and the energy of each setup showed that the ferromagnetic state was the ground-state configuration for the lattice. The analysis of electronic structure found both metallic and spin-polarized states, most of the magnetism being related to Fe and Dy atoms. Elastic constant analysis indicated that the material was both mechanically stable and ductile. Evaluating with BoltzTraP suggests that thermoelectric features show moderate efficiency along with spin features. It appears from this study that DyFe<sub>3</sub>Ni<sub>12</sub> has a stable structure and shows ferromagnetism which opens doors for magnetic and spin caloric uses.

Keyword: Intermetallic, Magnetic, Alloy, Intermetallic compound, Ternary, Dft, LSDA.

#### الملخص

في هذه الأطروحة، تم استخدام نظرية الكثافة الوظيفية (DFT) ضمن إطار LSDA، باستخدام برنامج WIEN2k، لدراسة الخصائص البنيوية والمغناطيسية والإلكترونية والميكانيكية والحرارية الكهربائية للمركب البينفلزي .DyFe3Ni12 أظهرت مقارنة الترتيبات المغناطيسية المختلفة والطاقة المرتبطة بكل منها أن الترتيب الفرومغناطيسي هو الترتيب الأساسي للشبكة البلورية. كشف تحليل البنية الإلكترونية عن وجود حالة معدنية ومستقطبة مغناطيسيًا، وكانت معظم الخصائص المغناطيسية مرتبطة بذرات الحديد (Fe) والديسبروسيوم .(Dy) كما أوضح تحليل الثوابت المرنة أن المركب يتمتع بثبات ميكانيكي وقابلية للانسياب وأظهرت نتائج الحسابات باستخدام BoltzTraPأن الخصائص الحرارية الكهربائية تظهر كفاءة معتدلة مصحوبة بسلوك معتمد على الاستقطاب المغناطيسي. تشير هذه الدراسة إلى أن المركب DyFe3Ni12 يتمتع بتركيب مستقر وصفات فرومغناطيسية، مما يجعله مرشحًا واعدًا لتطبيقات مغناطيسية وحرارية مغناطيسية مستقبلية.

الكلمات المفتاحية: بينفلزي، مغناطيسي، سبيكة، مركب بينفلزي، ثلاثي العناصر، نظرية الكثافة الوظيفية (DFT) ، تقريب الكثافة المحلية للسبين (LSDA) .

#### **RESUME:**

Dans ce travail de thèse, la Théorie de la Fonctionnelle de la Densité (DFT), dans le cadre de l'approximation LSDA, et mise en œuvre via le code WIEN2k, a été utilisée pour étudier les propriétés structurales, magnétiques, électroniques, élastiques et thermoélectriques du composé intermétallique DyFe<sub>3</sub>Ni<sub>12</sub>. Une comparaison des différentes configurations magnétiques et de leurs énergies respectives a montré que l'état ferromagnétique est la configuration fondamentale du réseau cristallin. L'analyse de la structure électronique a révélé un comportement à la fois métallique et polarisé en spin, la majorité du magnétisme provenant des atomes de fer (Fe) et de dysprosium (Dy). L'étude des constantes élastiques a montré que le matériau est mécaniquement stable et ductile. L'évaluation des propriétés thermoélectriques à l'aide du code BoltzTraP a mis en évidence une efficacité modérée, avec une dépendance notable au spin dans les phénomènes de transport. Cette étude suggère que DyFe<sub>3</sub>Ni<sub>12</sub> est un composé structurellement stable et ferromagnétique, offrant des perspectives intéressantes pour des applications magnétiques et calorico-spiniques.

*Mots-clés*: Intermétallique, Magnétique, Alliage, Composé intermétallique, Ternaire, DFT (Théorie de la fonctionnelle de la densité), LSDA (Approximation locale de la densité de spin)

#### **SUMMARY**

GENERAL INTRODUCTION
REFERENCES
CHAPTER 01: THE INTERMETALLIC COMPOUNDS
1.1 INTRODUCTION ABOUT INTERMETALLICS
1.2 STRUCTURE OF INTERMETALLICS
1.3 INTERMETALLIC PHASES
1.3.1 LAVES PHASES20
1.3.1.1 STABILITY AND SITE PREFERENCE21
1.3.1.2 IMPORTANCE OF LAVES PHASES
1.3.2 HEUSLER PHASES22
1.3.2.1 PROPERTIES OF HUSLER PHASES
1.3.2.2 D-METAL HEUSLER ALLOYS
1.3.2.3 HALF-HEUSLER ALLOYS
1.3.2.4 BINARY HEUSLER ALLOYS25
1.3.2.5 INVERSE HEUSLER ALLOYS
1.3.2.6 QUATERNARY HEUSLER ALLOYS27
1.3.3 ZINTL PHASES
1.3.3.1 d <sup>0</sup> TRANSITION METAL ZINTL PHASES

1.3.4 HUME-ROTHERY PHASES
1.4 METHODS OF ALLOYING INTERMETALLIC COMPOUND 29
1.5 THE RARE-EARTH INTERMETALLICS
1.5.1 HYDROGEN STORAGE MATERIALS30
1.6 PROPRIETIES OF INTERMETALLIC
1.6.1 MAGNETIC INTERMETALLICS
1.6.2 SUPERCONDUCTIVITY32
1.6.3 THERMOELECTRIC PROPRIETES
1.6.4 BATTERY MATERIALS34
1.7 SYNTHESIS METHODS FOR INTERMETALLIC COMPOUNDS33
1.7.1 SOLID-STATE SYNTHESIS
1.7.2 SELF-PROPAGATING SYNTHESIS
1.7.3 WET-CHEMICAL SYNTHESIS
1.7.4 GALVANIC REPLACEMENT SYNTHESIS
1.7.5 ELECTRODEPOSITION
1.7.6 DEALLOYING
1.7.5 BALL MAILLING
REFERENCES
CHAPTER 02: ELECTRONIC STRUCTURE THEORY AND WIEN2K CODE
2.1 INTRODUCTION

2.2 SOLVING SCHRÖDINGER'S EQUATION FOR A CRYSTALLINE SOLID47
2.2.3 THE BORN-OPPENHEIMER APPROXIMATION48
2.2.4 HARTREE APPROXIMATION49
2.2.5 HARTREE-FOCK APPROXIMATION (1930)50
2.3 DENSITY FUNCTIONAL THEORY DFT
2.3.1 THE TWO THEOREMS OF HOHENBERG AND KOHN51
2.3.1.A FIRST HOHENBERG-KOHN THEOREM51
2.3.1.B SECOND HOHENBERG-KOHN THEOREM52
2.3.2 KOHN-SHAM EQUATIONS (ORBITAL APPROACH)52
2.3.3 EXCHANGE RATE PROCESSING AND CORRELATION54
2.3.3.A LOCAL DENSITY APPROXIMATION (LDA)55
2.3.3.B GENERALIZED GRADIENT APPROXIMATION (GGA)55
2.3.3.C MBJ APPROXIMATION55
2.4 THE LINEARIZED AUGMENTED PLANE WAVE METHOD (FP-LAPW)56
2.4.1 INTRODUCTION56
2.4.2. AUGMENTED PLANE WAVE (APW) METHOD56
2.5 THE WIEN2K PACKAGE59
REFERENCES63
CHAPTER 03: RESULTS AND DISCUSSION

3.1 INTRODUCTION
3.2 METHOD OF CALCULATION66
3.3 STRUCTURAL DATA67
3.4 MAGNETIC RESULTS70
3.5 ELECTRONIC STRUCTURES71
3.5.1 PERTIAL DENSITY OF STATES
3.5.2 TOTAL DOS
3.5.3 BAND STRUCTURE
3.6 ELASTIC PROPERTIES75
3.7 THERMOELECTRIC RESULT79
REFERENCES
GENERAL CONCLUSION

#### LISTE OF TABLES

Table 3.1: Atomic position of Dysprosium, Nickel, Iron in DyFe <sub>3</sub> Ni <sub>12</sub> and FeNi <sub>3</sub>	67
Table 3.2: The structural result after getting minimal energy by using Birch-	Murnaghen
equation	70
Table 3.3: Magnetic data of the intermetallic DyFe <sub>3</sub> Ni <sub>12</sub> And FeNi <sub>3</sub>	70
Table 3.4: Values of elastic proprieties of DyFe <sub>3</sub> Ni <sub>12</sub> And FeNi <sub>3</sub>	78

#### LISTE OF FIGURES

Figure 1.1: Cr11Ge19 Compound Appearance
Figure 1.2: Cubic intermetallic structure type AB2
Figure 1.3: Binary Laves crystal structures. 3D representations of (a) the C14 (MgZn <sub>2</sub> ),
(b) the C15 (MgCu <sub>2</sub> ), and (c) the C36 (MgNi <sub>2</sub> ) structures. This figure represents a C14
structure and it shows its projection along the [ $1\overline{120}$ ] axis. The C15 structure displays its
configuration when observed through the [110] projection. The C36 structure
demonstrates this view direction down the [1120] projection. The viewer can access
interactive 3D representations of the three Laves phases in Supplementary Data 1-3 [8].
21
Figure 1.4: (a) The crystal structure of half-Heusler and (b) full-Heusler alloys. A half-
Heusler alloy consists of XYZ composition and a full-Heusler alloy adds a second Y2-site
atom to its crystals thereby becoming XY2Z material [11].
Figure 1.5: Periodic table of elements. The diverse creation of Heusler materials becomes
possible through various piece combinations according to the established color system
[ <b>12</b> ].
Figure 1.6: Chemical elements and hybridization differences between conventional and
all-d-metal Heusler alloys [15].
Figure 1.7: The binary X <sub>3</sub> Z Heusler structure places the X atoms in the green positions,
while the Z atoms are located in the blue positions [19].
Figure 1.8: Differences in structure between (a) full-Heusler alloys and (b) inverse-
Heusler alloys [21].
Figure 1.9: The structure of the equiatomic quaternary Heusler alloy with space group
F-43m (216) features atoms occupying the Wyckoff positions a, b, c, and d, represented
by green, red, blue, and yellow spheres, respectively [24].
Figure 1.10: The [NbAs 5] cluster in K 6 NbAs 5 exists in two bonding structures where
(a) Nb bonds with five As atoms and (b) Nb connects to an As-terminated [NbAs 4]
tetrahedron. The two elements appearing as light and dark spheres correspond to Nb
and As [27].

Figure 1.11: Temperature dependence of the magnetic susceptibility of TaRhGe,	
Ca2Pd2In, and LiRuSn4.	31
Figure 1.12: Schematic changes in the electrical resistivity (R), magnetic susceptibility	y
(χ), and heat capacity (Cp) during the superconducting phase transition [37].	33
Figure 1.13: a Schematic diagram for synthesis of CdS films using chemical b	ath
deposition technique. b Schematic of layer-by-layer CdTe NCs-CdS heterojunctions so	olar
cell device [45].	36
Figure 1.14: Substitution of copper monolayer on a noble metal M'noble substrate by	the
second noble metal M'noble is shown in schematic A. Schematic B shows the adsorption	n of
$M_{\text{noble}}$ on a reactive metal M substrate, followed by etching the metal atoms from	the
substrate side [47].	37
Figure 1.15: Schematic of an electrodeposition process [49].	38
Figure 1.16: A schematic shows the liquid metal dealloying Process [51].	39
Figure 2.1: Distribution of the unit cell, an interstitial region and spherical regions: $\boldsymbol{\alpha}$	
and $\beta$ spheres of muffin-tin rays and respectively $R\alpha R\beta$ .	57
Figure 2.2: Program organization chart in WIEN2k	60
Figure 3.1: (A) The atomic structure of DyFe <sub>3</sub> Ni <sub>12</sub> (B) The atomic structure of FeNi <sub>3</sub>	68
Figure 3.2: Volume optimization curve shows the 3 states (Antiferromagnetic Green li	ine,
Ferromagnetic Red line and non-magnetic blue line).	69
Figure 3.3: Shows the curves of density of state of DyFe3Ni12, (a) represent the iron-F	<sup>r</sup> e
curve, (b) illustrate the Nickel-Ni curve, (c) show the Dysprosium-Dy curve and (d) the	e
total dos of DyFe3Ni12	71
Figure 3.4: The band structure of DyFe3Ni12 with (a) represent spin up bands and the	e
(b) show the spin down bands and the both attached with dos curves.	74
Figure 3.5: The conductivity the electrical $\sigma$ (a) and Seebeck coefficient S (b), thermal	
conductivity κ0 (c) curves.	80
Figure 3.6: The curves of Power factor PF (a) and figure of merit ZT (b) with both spi	ins

# GENERAL INTRODUCTION

#### **General introduction**

The materials comprising the external world are comprised of particular particles, with a submicroscopic size. Their behaviors are based on atomic theories. States of organization of materials vary from complete disorder of atoms or indeed restitution of materials to order. from molecules of a gas under weak pressure to the approach to the almost full monocrystal order of atoms. In this context, materials solids handled by mankind to produce items that form basis of his living environment [1]. More typically, materials are identified along their most common characteristics, high mechanical strength materials, electricity conductors, permanent magnets etc. The classification of solid materials based on their physical properties, chemical composition and the privileged crystal structures gets advanced by researchers continually. Materials whose classes include metals, ceramics, minerals and semiconductors are characterized by the respective atoms they contain and the orderly orientation of these atoms in their crystal lattices. However, often researchers seek a way to enhance the amount and to modify properties of a given material by combining and alloying materials. This knowledge is important for the contemporary technology as it allows developing new materials with the desired properties and a high efficiency.

Our discussion is aiming towards the intermetallic compound, which are usually thought of as a type of materials for the class in between the metals and ceramics, whereas the link is in term of the blend between metal and covalent phases [2]. The designation of the intermetallic phases and compounds produced by the combination of several different metals has been applied in the term "intermetallic" to represent a large class of materials [3]. Very frequently, intermetallic compounds are rigid, i.e. they are hard, brittle and strong and normally possess a comparatively high chemically (good corrosion resistance). In addition, they are high melted and electrically conductive with a commonly greater order of magnitude than that of pure transition metals [4]. In the first chapter of this thesis, we note the types of intermetallic compounds and their proprieties given in detail. In chapter 2 we take deeper insight into behavior of intermetallic systems and here theoretical and computational techniques are of particular importance. Among these, there has emerged a comprehensive and widely used quantum mechanical method to study the electronic structure of solids the density functional theory (DFT) and we talk about Wien2k code and their tools which It employs density functional theory to calculate the electronic structure of a solid. After all we concentrate on the research of an intermetallic compound DyFe<sub>3</sub>N<sub>12</sub> where we intend

to investigate its structural electronic and magnetic properties, mechanical and thermoelectric characteristics. A strong version of the Full-Potential Linearized Augmented Plane Wave (FP-LAPW) method implemented under DFT via the WIEN2k code; we carry out detailed calculations to comprehend the behavior of this intricate compound. The results concluded in the final chapter impart useful theoretical information that can guide future experimental and technological exploration on rare-earth—transition metal nitrides. Finally, we finished the thesis with a conclusion on the general values and properties of our material, and its uses in application areas where it can be applied.

#### **References:**

- [1] Mercier, Jean P., et al. "Materials." *Elsevier eBooks*, 2002, pp. 1–16. https://doi.org/10.1016/b978-2-84299-286-6.50007-x.
- [2] Smallman, R. E., and R. J. Bishop. "Modern Alloy Developments." *Elsevier eBooks*, 1999, pp. 297–319. https://doi.org/10.1016/b978-075064564-5/50009-4.
- [3] Perez-Prado, M. -t., and M. E. Kassner. "Creep of Intermetallic." Elsevier eBooks, 2015, pp. 189–232. https://doi.org/10.1016/b978-0-08-099427-7.00009-8.
- [4] Günter Gottstein "Physikalische Grundlagen Der Materialkunde." Springer-Lehrbuch, 2007, https://doi.org/10.1007/978-3-540-71105-6.

# CHAPTER I:

# The Intermetallic Compounds

#### 1.1 Introduction about intermetallics:

The intermetallic compound group consists of two or more elements which combine through specific ratios to create ordered crystal structures of metallic or metalloid nature. Intermetallic compounds diverge from traditional compounds because they do not need to maintain charge balance and thus create a wide range of possible compositions especially during three or fourelement combinations. Such materials demonstrate special properties beyond component behavior which include magnetic qualities and also exhibit superconducting properties and produce magnetocaloric and thermoelectric effects. The combination of rare earth elements with transition metals generates specialized magnetic properties because the metals activate mutual interactions. Carbon reveals vital importance in synthetic materials since its small electronegative nature enables the development of  $C^{4-}$  and diatomic  $C_2^{2-}$  (acetylide) and  $C_2^{4-}$  (ethynide) species that can either enter interstitial rare earth ion spaces or bond with transition metals [1]. Rare earth element intermetallic exhibit a wide array of intriguing characteristics because of their electric conduction capabilities along with the magnetic properties of their rare earth ion components. The structural complexity of ternary and quaternary phases enables both doping and site-specific substitution through their increased complexity making them suitable for property enhancement. Intermetallic compounds lack average charge balance which makes their compositional adjustments possible without adherence to neutrality rules.

#### 1.2 Structure of intermetallics:

Phase diagrams featuring binary systems show intermetallic as either single lines between components or as substances that exist between pure metals and do not reach their endpoints. Scientists study ordered binary or multicomponent intermetallic alloys with multiphase microstructures because they want to develop materials which withstand both extreme conditions and high temperatures and weigh less. An impervious Al<sub>2</sub>O<sub>3</sub> or SiO<sub>2</sub> scale develops to provide excellent oxidation protection when the temperature exceeds 1000°C within aluminide- or silicide-based intermetallic systems [2]. It's stand as the least studied category of inorganic solids concerning bonding characteristics. The bonding mechanisms of ionically or covalently bonded compounds differ from those of the compounds, it is nearly impossible to apply simple heuristic concepts to reliably predict compositions or structural characteristics based on the elements

involved or the valence electron concentration (VEC) [3] per atom. The Fermi liquid theory and traditional models do not provide sufficient accuracy when describing electrical conductivity and magnetic susceptibility in basic physical properties. The impact of chemical bonding factors depends strongly on both composition changes and the nature of the elements involved because these factors change steadily across a wide range of conditions [4].



Figure 1.1: Cr11Ge19 Compound Appearance

Intermetallic compounds exist in stoichiometric compositions matching standard metal valences as well as more or less variable compositions in phase diagrams. A phase range defines the systematic modification limits of the metal percentages that make up a material.

#### 1.3 Intermetallic phases:

- Laves phases (type AB2, e.g. CaMg2)
- Heusler phases (ABC, A2BC, e.g. Cu2MnAl)
- Zintl phases (type AB, between alkaline and alkaline-earth metals and electronegative elements of the 13th to 16th main group, e.g. NaSi)
- Hum-Rothery phases, characterized by their fixed valency-electron concentration

#### 1.3.1 Laves phases:

Fritz Laves (1906-1978) established vital observations about intermetallic compound crystallography between cubic MgCu<sub>2</sub> structures and hexagonal MgZn<sub>2</sub> and MgNi<sub>2</sub> types when he published his work in the 1930s [5]. According to Gustav E.R. Schulze "Laves phases" became the initial designation for this AB<sub>2</sub> intermetallic compound group [6Laves phases exist as intermetallic compounds which follow the AB<sub>2</sub> stoichiometric ratio under atomic size ratio conditions between 1.05 and 1.67. The three structural classes of Laves phases include cubic MgCu<sub>2</sub> (C15) and hexagonal MgZn<sub>2</sub> (C14) and hexagonal MgNi<sub>2</sub> (C36). A atom in these structures exist in similar positions to diamond or hexagonal diamond structures as well as related configurations whereas B atoms fill tetrahedral positions that encircle the A atoms. The compounds develop tetrahedral close-packed structures topologically when the atomic size ratio between A and B matches 1.225 because this ratio produces an overall packing efficiency of 0.71 [7].

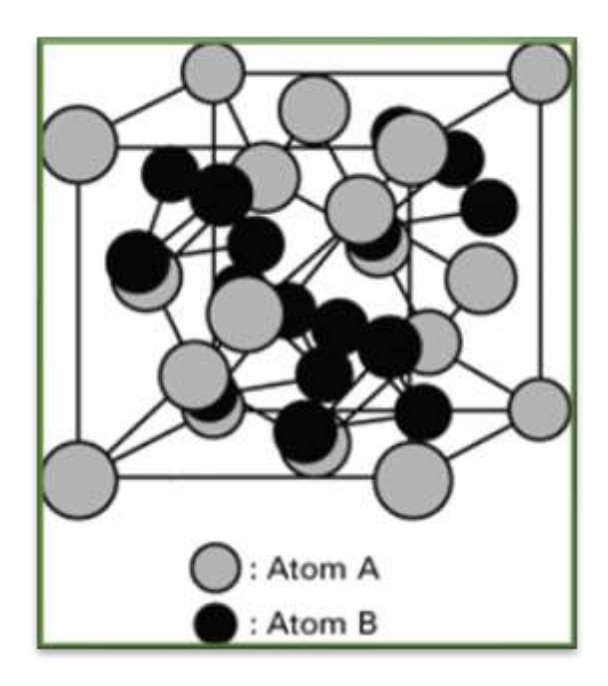


Figure 1.2: Cubic intermetallics structure type AB2

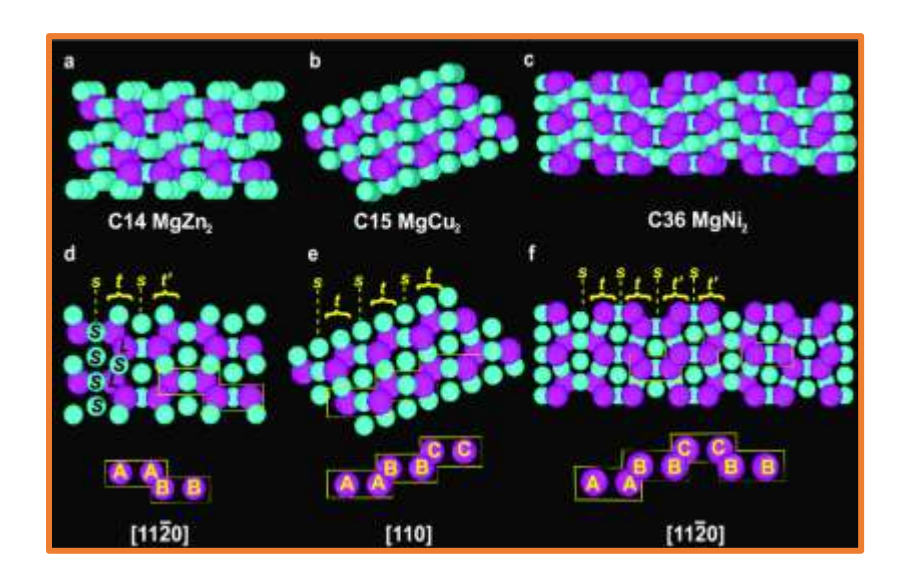


Figure 1.3: Binary Laves crystal structures. 3D representations of (a) the C14 (MgZn<sub>2</sub>), (b) the C15 (MgCu<sub>2</sub>), and (c) the C36 (MgNi<sub>2</sub>) structures. This figure represents a C14 structure and it shows its projection along the [1120] axis. The C15 structure displays its configuration when observed through the [110] projection. The C36 structure demonstrates this view direction down the [1120] projection. The viewer can access interactive 3D representations of the three Laves phases in Supplementary Data 1-3 [8].

#### 1.3.1.1 Stability and site preference:

The declaration that a Laves phase AB<sub>2</sub> exists indicates the phase maintains thermodynamic stability within specific conditions or it exists because of thermodynamic or kinetic production processes. Phase formation relies essentially on both thermodynamic stability between elements and the simultaneous competition with alternative phases regarding thermodynamic and kinetic criteria. The manifestation of Laves phase AB<sub>2</sub> might be prevented due to its inability to compete against more stable phases or phases that form faster according to first-principles calculations. The limitations for predicting such phase stability exist when strictly evaluating the system based on composition alone because additional possible states must be factored into calculations.

#### 1.3.1.2 Importance of laves phases:

The functional uses of Laves phases extend into an exceptionally diverse set of successful applications. Hydraloy seeks hydrogen storage while Terfenol acts as a magneto-mechanical sensor and actuator along with Tribaloy serving as wear-resistant coating for harsh settings

(Tribaloy). Laves phases receive fresh interest as structural components for high-temperature steel creep strength enhancement through successful development of new alloy design methods.

#### 1.3.2 Heusler phases:

Three members of the Heusler family Conrad and Friedrich (Fritz) and Otto Heusler [9] independently contributed to the development of Heusler alloys into a magnetic material family that uses non-magnetic components for their wide range of useful functions. Their investigations first started when they sought out a different bronze alloy. The "Isabelle" Plant in Dillenburg, Germany began producing technically iron-free alloys in 1876 during the initial phase of research that eventually resulted in Heusler alloy discovery. Heusler alloys resulted from accidental discovery at the beginning of the twentieth century but have become significant materials for outstanding functional applications in both spintronics and thermoelectric devices throughout the twenty-first century.

The defining structural trait of Heusler alloys describes the arrangement between their face-centered cubic (FCC) superlattices and body-centered cubic (BCC) unit cell [10]. The atomic arrangements in Heusler alloys produce unique atomic divisions which are absent from pure elements and disordered solid solutions leading to potential discoveries of new material properties. The ferromagnetic properties of Cu<sub>2</sub>MnSn emerged as the alloy exhibited magnetic behavior though its components lacked ferromagnetic behavior in isolated states. Scientists have expanded Heusler alloys into a diverse group of materials through Full Heusler alloys which follow the stoichiometric formula X<sub>2</sub>Y<sub>1</sub>Z<sub>1</sub>.

Half Heusler alloys and Inverse Heusler and Binary Heusler together with Quaternary Heusler alloys represent different subclasses of Heusler alloys that follow stoichiometries  $X_1Y_1Z_1$  and  $X_2Y_2Z_2$  to  $X_1X_2Y_1Z_2$ . The structural and functional characteristics among Heusler compounds subclasses prove unique thus expanding the versatility available through these compounds.

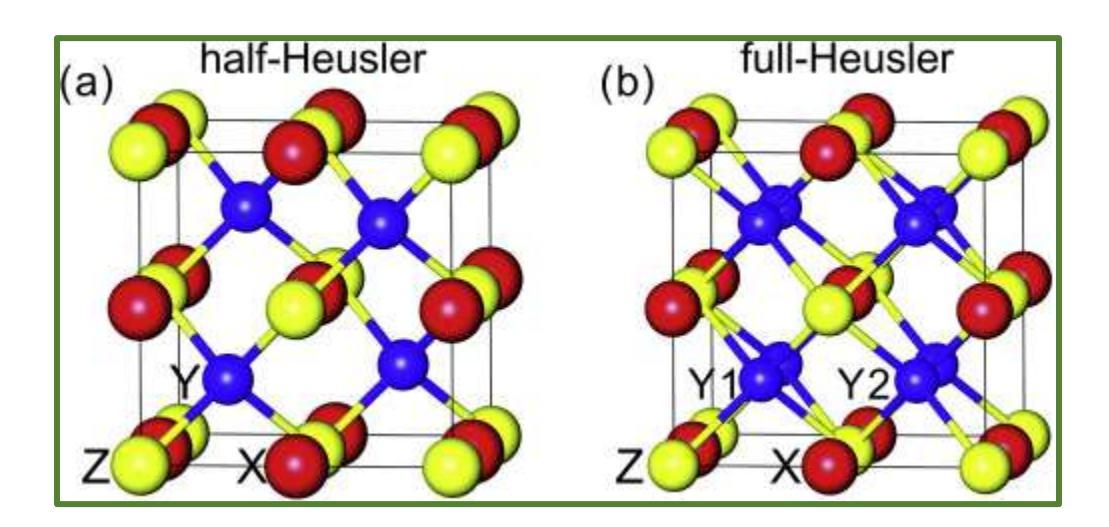


**Figure 1.4:** (a) The crystal structure of half-Heusler and (b) full-Heusler alloys. A half-Heusler alloy consists of XYZ composition and a full-Heusler alloy adds a second Y2-site atom to its crystals thereby becoming XY2Z material [11].

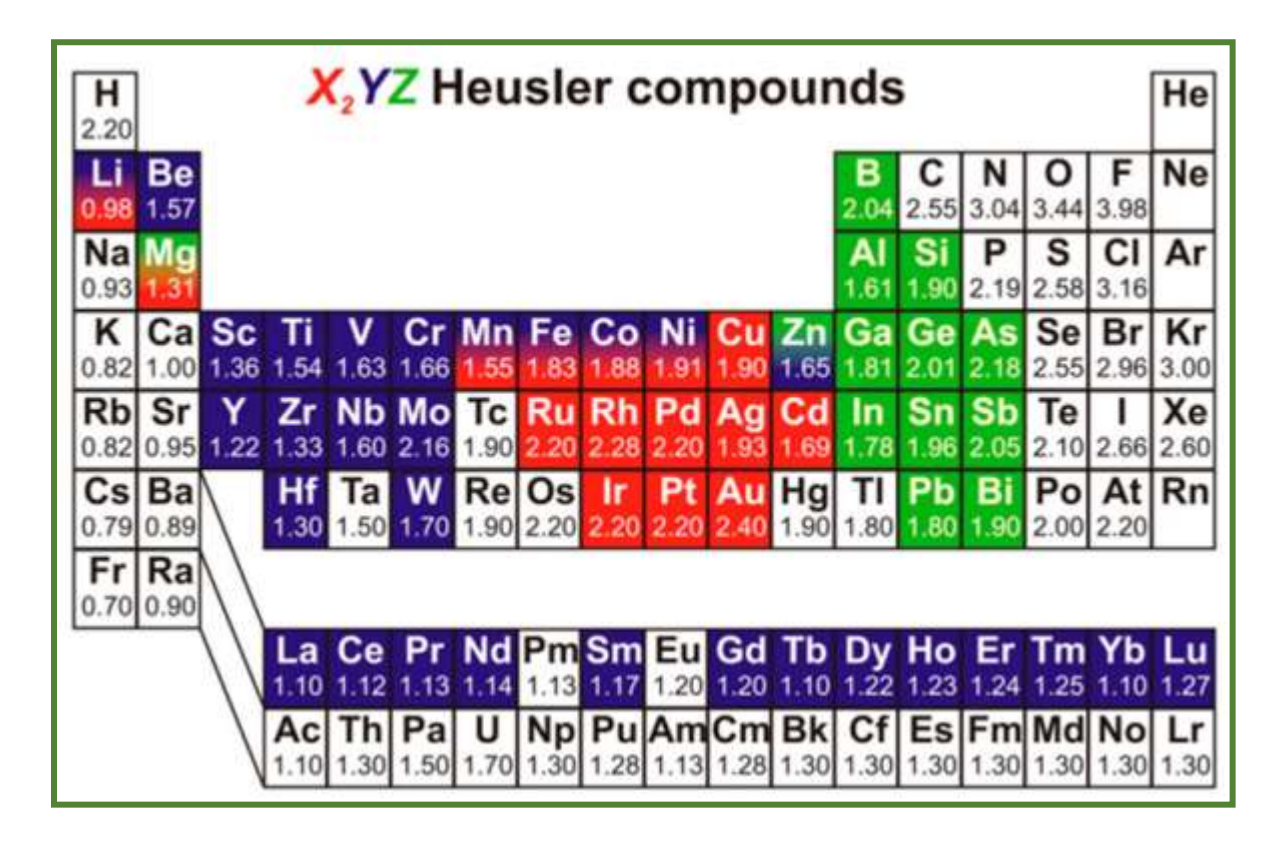


**Figure 1.5:** Periodic table of elements. The diverse creation of Heusler materials becomes possible through various piece combinations according to the established color system [12].

#### 1.3.2.1 Properties of Heusler phases:

Heusler alloys demonstrate special properties including the magnetic shape-memory effect according to [13] that enables these materials to change shape reversibly under magnetic field influence. The exceptional characteristic of Heusler alloys enables these materials to find crucial use in advanced functional applications.

In addition to their other properties, Heusler alloys can also exhibit spin-glass behavior [14], a phenomenon where the magnetic moments become frozen in random orientations below a certain temperature.

#### 1.3.2.2 d-metal Heusler alloys:

All-d-metal Heusler alloys consist only of transition metals while Z atoms take place at the D sites as transition metals. None of the main-group metals are present in the structure of these unique alloys. The entire composition of X Y and Z atoms which exclusively consists of transition metals distinguishes them from standard Heusler alloys while providing unique properties for evolving technology applications. The compounds display complete d-electron configurations in the chemical makeup of their constituent metals.

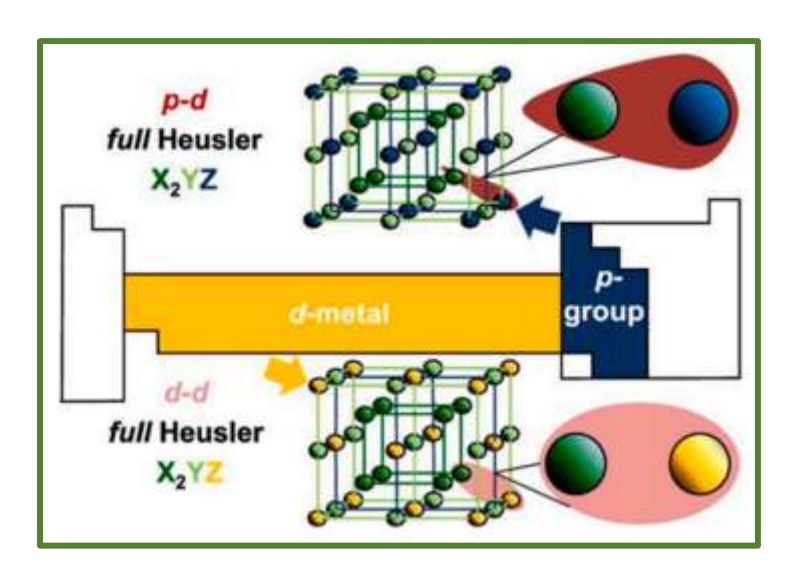


**Figure 1.6:** Chemical elements and hybridization differences between conventional and all-d-metal Heusler alloys [15].

#### 1.3.2.3 Half-Heusler alloys:

The general composition of Half-Heusler (HH) alloys follows XYZ with transition metals occupying X and Y spots yet the Z position contains a main group element. Static structures of these alloys adopt the MgAgAs crystal pattern which belongs to the F-43m space group. The Half-Heusler alloy's structure contains four individual face-centered cubic (fcc) sublattices that give these materials their distinct structural characteristics [16]. The three atomic positions in Half-Heusler alloys show the Z atom at (0, 0, 0), the Y atom at  $(\frac{1}{4}, \frac{1}{4}, \frac{1}{4})$ , and the X atom at  $(\frac{1}{2}, \frac{1}{2})$  as shown in Fig. 4(a). The atom position at  $(\frac{3}{4}, \frac{3}{4}, \frac{3}{4})$  within the fourth face-centered cubic sublattice remains empty.

#### 1.3.2.4 Binary Heusler alloys:

The chemical formula of Binary Heusler alloys follows X<sub>3</sub>Z which consists of transition metals X and main group element Z [17]. Binary Heusler alloys create a crystal structure with face-centered cubic (FCC) symmetry of the D0<sub>3</sub>-type and they hold the identical space group Fm-3m similar to full Heusler alloys. Identity between all X and Y elements in full-Heusler compounds leads to the formation of the D0<sub>3</sub>-type structure. In this arrangement each of the three X atoms X1, X2 and X3 occupies the crystal positions (1/4, 1/4, 1/4), (1/2, 1/2, 1/2), and (3/4, 3/4), respectively, and the Z atoms are located at (0, 0, 0). The crystal pattern creates ferromagnetic behavior between X<sub>1</sub> and X<sub>2</sub> and X<sub>3</sub> because X<sub>1</sub> and X<sub>3</sub> have identical positions in the structure [18].

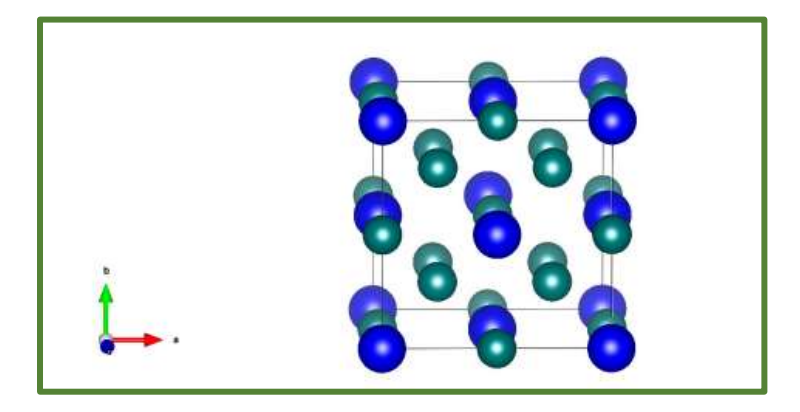


**Figure 1.7:** The binary X<sub>3</sub>Z Heusler structure places the X atoms in the green positions, while the Z atoms are located in the blue positions [19].

#### 1.3.2.5 Inverse Heusler alloys:

The transformation of full-Heusler alloys yields inverse-Heusler alloys through a rearrangement process for the atomic positions. The X<sub>2</sub>YZ chemical composition of full-Heusler alloys transforms to XYZ in inverse-Heusler alloys since the X and Y atomic sequence exchanges leading to modified crystal structure developments. Moving the X and Y atomic positions creates essential modifications in electronic structure and magnetism of the material. Transition metal atom site preference is determined by the number of valence electrons (ZV) they possess. When ZV(Y) exceeds ZV(X) the X atoms configure at sites (½, ½, ½) and (¾, ¾, ¾) but Y and Z atoms occupy positions (¼, ¼, ¼) and (0, 0, 0) respectively for X and Y atoms within the same periodic table period. The XA-type structure develops through this arrangement which belongs to space group F43m [20].

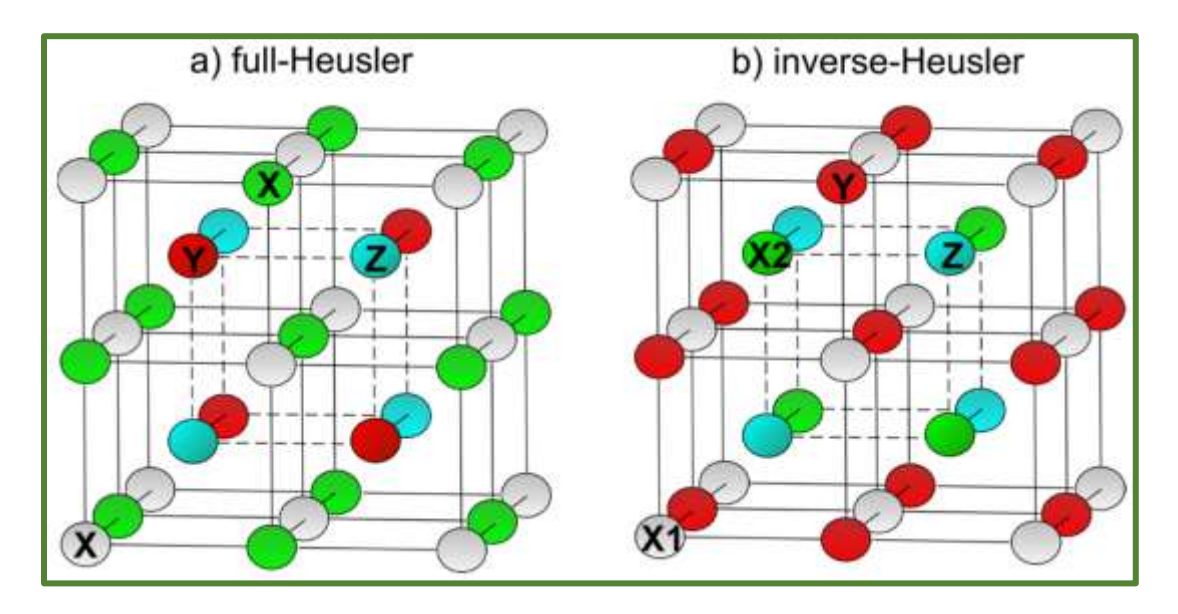


**Figure 1.8:** Differences in structure between (a) full-Heusler alloys and (b) inverse-Heusler alloys [21].

#### 1.3.2.6 Quaternary Heusler alloys:

A quaternary Heusler structure with unique structural symmetry (space group: F-43m, 216) is formed when different atoms (XX'YZ) occupy each of the sublattices. The resulting structure is referred to as the LiMgPdSn type, or Y-type [22]. The disorder scattering from random Y and Y' distribution reduces the spin diffusion length in equiatomic quaternary Heusler alloys more than in pseudo-ternary alloys X<sub>2</sub>Y<sub>1-x</sub>Y'<sub>x</sub>Z. The different length of spin diffusion brings unique benefits for particular uses. The power dissipation in devices using XX'YZ structures is expected to be low because disorder scattering does not occur in this system [23].

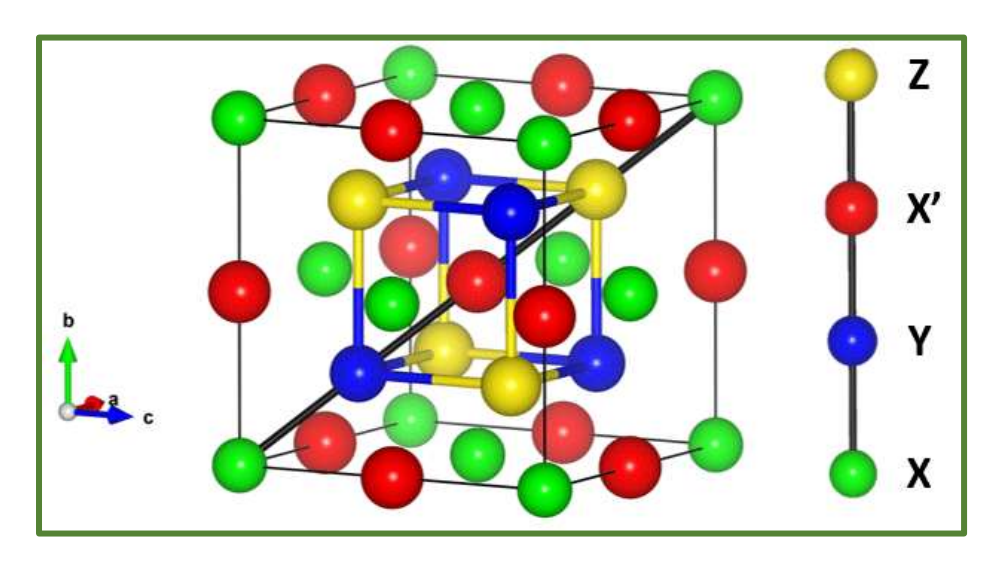


**Figure 1.9:** The structure of the equiatomic quaternary Heusler alloy with space group F-43m (216) features atoms occupying the Wyckoff positions a, b, c, and d, represented by green, red, blue, and yellow spheres, respectively [24].

#### 1.3.3 Zintl phases:

The field of intermetallic compounds features a specific group known as Zintl phases that carries the name of Eduard Zintl (1898–1941). Zintl phases constitute a division of intermetallic where bond explanations follow traditional chemical definitions through ionic and covalent bonding patterns. During these phases electropositive cations give electrons to more electronegative elements through ionic bonding. When electrons are donated between elements it leads to the creation of polyanionic networks or clusters which bond through covalent or polar

covalent mechanisms and isolated anionic species that reach complete octet stability. [25-26] The AB<sub>2</sub>C<sub>2</sub>-type compounds represent among many Zintl phase families that use different elements. The compounds comprise A elements as alkaline-earth or rare-earth metals including Mg, Ca, Sr, Ba, Eu, Yb and B elements from transitioning metals or main-group components including Zn, Cd, Mg, Mn, Al with C elements from the group IV/V elements Si, Sb, Bi. The molecules crystallize inside CaAl<sub>2</sub>Si<sub>2</sub> arrangements that possess the P-3 m1 symmetry group.

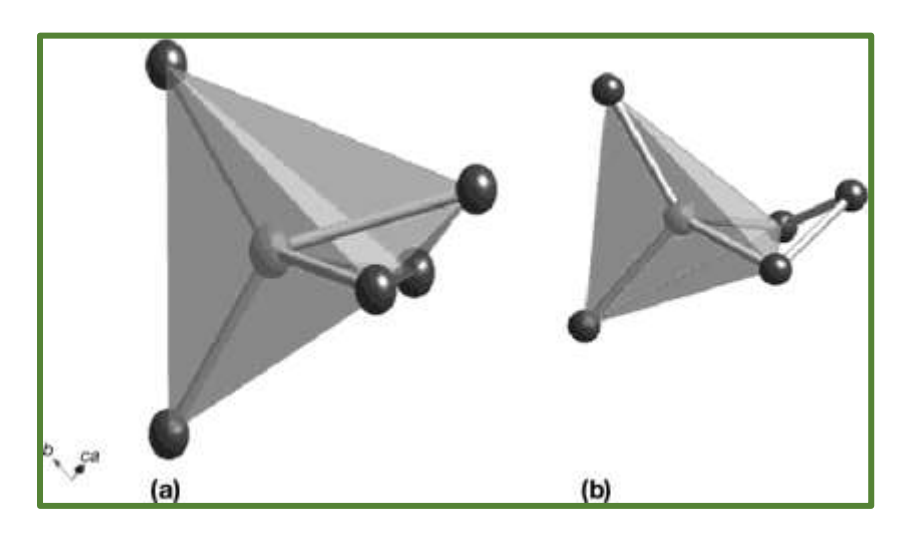


**Figure 1.10 :** The [NbAs 5] cluster in K 6 NbAs 5 exists in two bonding structures where (a) Nb bonds with five **As** atoms and (b) **Nb** connects to an As-terminated [NbAs 4] tetrahedron. The two elements appearing as light and dark spheres correspond to Nb and As [27].

#### 1.3.3.1 D<sup>0</sup> transition metal Zintl phases:

Available research on Zintl phases that use early transition metals remains scarce in number. Compounds such as [Na<sub>5</sub>MAs<sub>3</sub>] (M = Ti, Hf) and Na<sub>8</sub>TiAs<sub>4</sub> originated among the first group of Zintl phases with early transition metal analogs because they crystallize in the Na<sub>5</sub>SiP<sub>3</sub> and Na<sub>8</sub>SnSb<sub>4</sub> structure types. In their crystal structures alkali metal cations provide electrons to either edge-sharing [M<sub>2</sub>As] units made of [MAs<sub>4</sub>] tetrahedral segments or independent [MAs<sub>4</sub>] tetrahedral units [28].

#### 1.3.4 Hume Rothery phases:

In 1926 Hume-Rothery established through empirical studies that compounds like CuZn Cu<sub>3</sub>Al and Cu<sub>5</sub>Sn adopt the body-centered cubic (bcc) structure with 3/2 electrons per atom [29]. Research conducted on these compounds indicates that the value stems from their average valence electron count per atom. Regarding this formation process these metals have been classified as mono-, di-, tri-, and tetra-valent elements which indicates their capacity to donate one, two three and four outermost electrons from their free atoms respectively [30]. Mott and Jones [31] resolved the Hume-Rothery electron concentration rule in 1936 by examining the contact between the Fermi sphere and the specific planes of Brillouin zones that match different phases. The theoretical framework provided understanding about electron concentration stability effects on crystal structures as a relation between Fermi surface geometry and Brillouin zone boundary positions. Raynor extended Hume-Rothery theory to s p alloys with transition metal atoms in its early development phase [32]. The prediction system for crystal structures using e/a average valence electrons per atom values could work for these alloys if negative valences were assigned to transition metal atoms. Raynor understood these observations as showing transition metal atoms carry a negatively charged state and all their d orbitals are occupied. Experimental evidence showed that this interpretation proved inappropriate because it indicated an excessive electrostatic energy did not match test results. Hume-Rothery phases are metallic alloys characterized by nearly free electrons, stabilized by their band energy. Hume-Rothery outlined the following empirical conditions for their formation:

- Small atomic radius difference: The difference between the atomic radii of constituents A and B, denoted as  $R_A$  and  $R_B$ , should be minimal, typically satisfying  $(RA RB)/RA \lesssim 0.15$ .
- Small electronegativity difference: The electronegativity difference between the constituents of the alloy should also be minimal.

These conditions ensure that the alloy components are compatible in terms of size and electronic structure, facilitating the formation of stable metallic phases.

#### 1.4 Methods of alloying intermetallic compound:

Alloying an intermetallic compound typically involves substituting certain elements within the compound to alter its properties. This process can be done by:

- **Substitutional Alloying:** Replacing some of the atoms in the intermetallic compound with different atoms. For example, substituting rare earth metals or transition metals to optimize magnetic properties.
- Interstitial Alloying: Introducing small atoms like B, C, or N into the spaces (interstices) between the atoms in the intermetallic lattice. This can enhance properties such as magnetic strengths.
- Controlled Processing: Using advanced processing techniques developed for other materials to achieve the desired alloy composition and structures.

#### 1.5 The rare-earth intermetallics:

Rare earth intermetallic compounds belong to the line compound category because their composition limits stretch across a minimal range. Producing rare earth elements poses preparation difficulties because these elements have high oxygen reactivity that causes adverse reactions when using conventional crucible materials. Several expert techniques for synthesizing rare earth intermetallic phases have emerged as a remedy to this concern (Herget and Domazer, 1975).

Research on rare earth intermetallic maintains practical value because their magnetic properties become exceptional after considering composition and crystal structure elements (Buschow 1980, 1991). The combination of SmCo and  $Sm_2Co_{17}$  led to the creation of rare earth permanent magnets (REPMs). The magnetic performance benefits of these magnets stem from their exceptional  $B \times Hmax$  value combined with high coercivity properties because B finds expression as magnetic induction and H defines magnetic field strength.

#### 1.5.1 Hydrogen storage materials:

In addition to their use as magnet materials, A large number of hydrogen absorption abilities exist within rare earth intermetallic phases, making them highly valuable for hydrogen storage

applications. Examples include compounds like RCo<sub>5</sub>, RFe<sub>2</sub>, and rare earth Laves phases, which have shown great potential in this field. Their ability to store hydrogen efficiently is of high interest for developing advanced energy storage systems.

#### 1.6 Proprieties of intermetallic:

#### 1.6.1 Magnetic intermetallics:

If a species possesses electron shells that remain completely filled then it lacks a permanent magnetic moment which leads to minimal magnetic susceptibility and produces small negative values similar to diamagnetic behavior [33]. which are repelled by magnetic fields. For simple ions and organic fragments, diamagnetism is well understood and can be calculated using standard increments. However, explaining diamagnetism in metals and intermetallic, like copper and silver, is more complex. Compounds such as Ca<sub>2</sub>Pd<sub>2</sub>In [34] and LiRuSn<sub>4</sub> [35] exhibit temperature-independent susceptibility down to 25 K, after which slight increases due to paramagnetic impurities are observed Fig.11. These compounds have negative susceptibility, indicating diamagnetism, despite their metallic conductivity, due to core diamagnetism offsetting Pauli susceptibility.

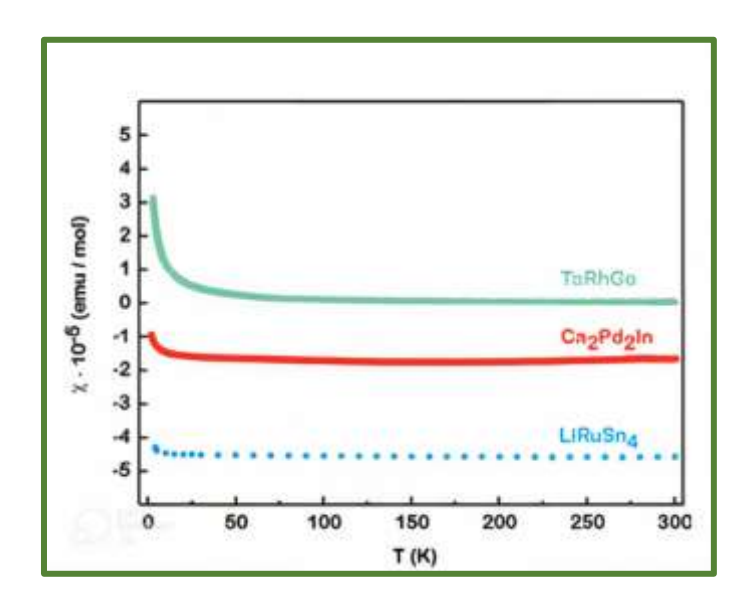


**Figure 1.11:** Temperature dependence of the magnetic susceptibility of TaRhGe, Ca2Pd2In, and LiRuSn4.

In conductive intermetallic compounds, both diamagnetic and paramagnetic effects are present. Para-magnetism, with stronger magnetic effects, occurs in materials with partially filled d- or f-shells and follows the Curie or Curie-Weiss law that's shown in Formula 1 and 2 In order. The magnetic moments align with external fields but are disrupted by thermal agitation, leading to temperature-dependent susceptibility. The paramagnetic Curie temperature ( $\theta$ ) helps indicate ferromagnetic or antiferromagnetic interactions, and the magnetic moment can be calculated using the Curie constant.

$$\chi = C/T \tag{1.1}$$

$$\chi = C / T - \theta \tag{1.2}$$

The expression describes the magnetic behavior under the Curie constant C along with paramagnetic Curie temperature  $\theta$  which reveals antiferromagnetic (negative  $\theta$ ) or ferromagnetic (positive  $\theta$ ) conditions.

Using the following formula scientists can determine the experimental magnetic moment of compounds:

$$\mu_{exp} = (8\mathcal{C})^{\frac{1}{2}} \tag{1.3}$$

#### 1.6.2 Superconductivity:

Superconductivity [36] becomes active in materials which develop zero electrical resistance and exclude magnetic fields underneath their critical temperature (Tc) while demonstrating a sudden increase in specific heat. The applications of superconductors in today's society mainly use their unique qualities of zero electrical resistance and magnetic field exclusion for the generation of high magnetic fields which leads to medical diagnostics by MRI technology and NMR spectrometer operations and high-energy particle accelerator use such as the Large Hadron Collider (LHC).

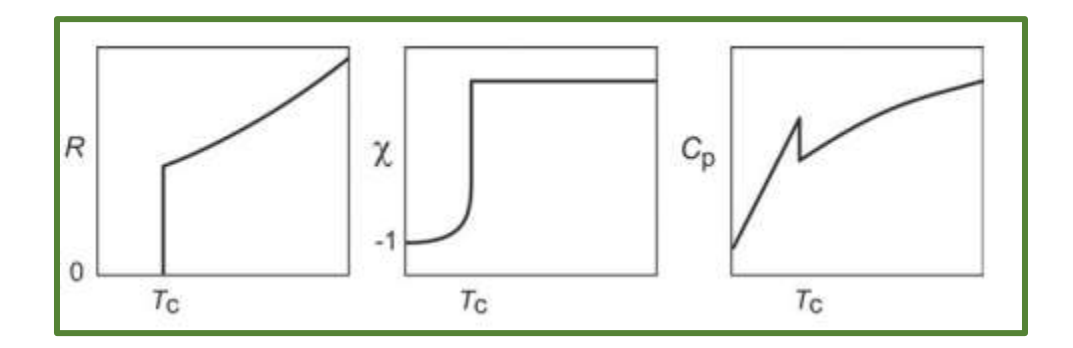


Figure 1.12: Schematic changes in the electrical resistivity (R), magnetic susceptibility ( $\chi$ ), and heat capacity (Cp) during the superconducting phase transition [37].

In 2006 researchers discovered superconductivity in intermetallic iron pnictides by using LaFePO which exists as tetragonal ZrCuSiAs-type structural material. Researchers did not show significant interest in the discovery because LaFePO exhibited a critical temperature of only 4 K [38]. The discovery of superconductivity at 26 K became possible after adding fluoride to LaFeAsO which triggered a dramatic shift in the scientific community [39].

#### 1.6.3 Thermoelectric proprieties:

The thermoelectric effect functions as a direct method to convert heat energy into electrical energy because of its critical role in alternative energy creation and waste heat recovery efficiency [40]. Thermoelectric devices operate based on the Seebeck effect, generating voltage (V) from a temperature gradient, and the Peltier effect, where current induces a temperature gradient. The Seebeck coefficient ( $\alpha$ ) quantifies this by relating the voltage generated to the temperature difference.:

$$\alpha = V / \Delta T \tag{1.4}$$

The measurement scale for Seebeck coefficients spans between  $-100~\mu\text{V/K}$  to  $+1000~\mu\text{V/K}$ . Products measuring under  $-100~\mu\text{V/K}$  belong to n-type materials and indicate electron dominance whereas values above  $+1000~\mu\text{V/K}$  signify p-type materials with hole-dominated charge carriers. A suitable thermoelectric material obtains high thermoelectricity resin (S) but maintains low electrical resistivity ( $\rho$ ) and thermal conductivity ( $\kappa$ ) that comprises electronic ( $\kappa$ e) and lattice ( $\kappa$ L) elements. The physical relationship that links these major parameters produces a

dimensionless figure of merit (ZT) which directly affects thermoelectric generator performance efficiency.

$$ZT = \frac{S^2T}{\rho(\kappa_e + \kappa_l)} \tag{1.5}$$

Zintl phase semiconducting intermetallic compounds, such as Zn<sub>4</sub>Sb<sub>3</sub>, have gained interest for their low thermal conductivity, which improves their thermoelectric properties. Zn<sub>4</sub>Sb<sub>3</sub>, in particular, shows glass-like thermal conductivity [41].

#### 1.6.4 Battery materials:

Intermetallic compounds are foundational materials in the field of energy materials. One important category includes binary and multinary metal hydrides, which are used for hydrogen storage and in metal hydride batteries. In these batteries, during the charging process, the metal (M) at the negative electrode reacts with hydrogen, following the reaction:

$$H_2O + M + e^- \rightarrow HO^- + MH$$
 (1.6)

Intermetallic lithium compounds play a crucial role in rechargeable lithium-ion batteries, forming the second group of important energy materials [42] Elemental lithium electrodes can lead to dendrite formation and short circuits, causing safety concerns due to lithium's low melting point. To mitigate these risks, binary intermetallic lithium compounds like silicides, stannides, and antimonides are employed.

#### 1.7 Synthesis methods for intermetallic compounds:

#### 1.7.1 Solid-state synthesis:

Solid-state synthesis mostly involves heating solid-state precursors to change the location of metal atoms and form IMCs. The main way to refine metals currently is by using the arc melting method which relies on creating a small spark by high voltage electricity to melt the metal. Most of this process depends on the use of an arc furnace. These characteristics of the arc melting technique are as follows: (i) the temperature achieved is high enough for the melting of most refractory materials (1980 °C); (ii) the shorter melting time (30–60 seconds) preserves the purity of elements; (iii) the intense arc mixes every part of the melt, resulting in a very homogeneous

liquid; and (iv) high-purity carbon-free gasses like argon can protect the liquid during melting. Up to now, arc-melting is the focus of most research on how to construct IMCs [43].

#### 1.7.2 Self-propagating synthesis:

SHS is the method by which a preform is included in the molten matrix phase. The reinforcement is formed in the molten metal when fast heat-producing reactions occur. As soon as the reaction begins, the heat produced breaks the model to help reinforce the molten matrix. A lot of researchers have experimented with TiC reinforced Mg-MMCs based on AZ91 alloy. Here, cold compacting was performed on Al-Ti-C preform and once complete, it was sintered. If a preform is submerged in molten magnesium, SHS begins and forms TiC particles simultaneously [44]. If the exothermic temperature and density of the cold compact preform or master alloy are right, SHS reaction can get started.

#### 1.7.3 Wet-chemical synthesis:

Preparing nanomaterials in solution by wet-chemical synthesis involves using chemical reactions in a solvent, among the oldest and most common ways. The method can be used to make various layered nanomaterials with low costs and at low temperatures. Because it works smoothly and is easy to repeat, wet-chemical synthesis is widely favored when making nanolayered materials with consistent size and thickness. Among the regular wet chemical approaches for assembling layered nanomaterials.

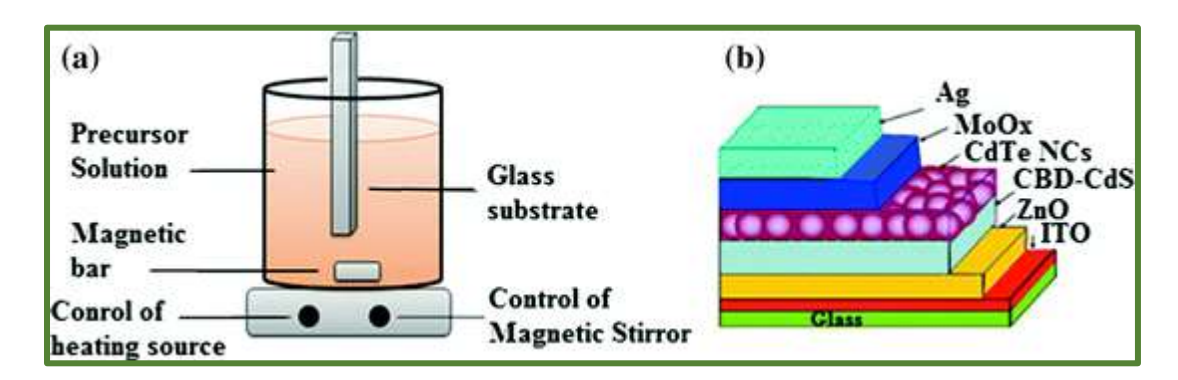


**Figure 1.13:** a Schematic diagram for synthesis of CdS films using chemical bath deposition technique. b Schematic of layer-by-layer CdTe NCs-CdS heterojunctions solar cell device [45].

#### 1.7.4 Galvanic replacement synthesis:

In galvanic replacement synthesis [46], atoms are stripped from the substrate because of oxidation and are dissolved in a solution. As the other, higher reducing material is electroplated onto the substrate, it is reduced by the solution. Two different reduction potentials in the redox pairs are the main reason for the spontaneity of these reactions. The use of both bulk and micro/nanostructured materials as substrates for galvanic replacement synthesis has been examined. Because of the tiny structures, micro/nanostructured materials achieve greater surface area which provides several quick benefits when compared with traditional electrosynthesis. Such materials can be prepared by mixing them together with the salt precursors in a usual chemical reaction solution. Like in an electrosynthesis, the material that reduces is often put straight down onto the substrate. While in electrosynthesis, both electrodes are in separate locations, connected by an electrolyte solution, for micro/nanostructured cathodic stripping, both the cathode and anode are embedded together even though each is in a unique location on the surface. By carrying out the reactions of oxidation and dissolution at various parts of the substrate and the reduction and deposition reactions together on the same surface, new atoms on the substrate can be grown into different nanostructured materials. Galvanic replacement synthesis has been used to make substrates out of crystalline, amorphous, metallic and nonmetallic materials. Depending on what the substrate is, the pattern of growth can vary, leading to several kinds of useful nanomaterials.

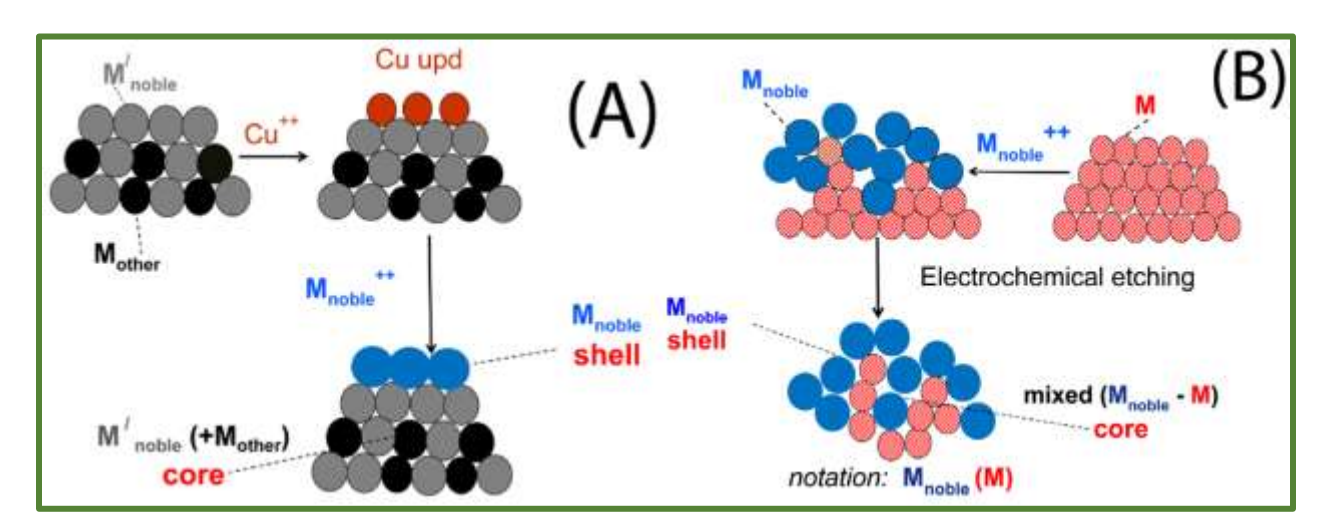


**Figure 1.14:** Substitution of copper monolayer on a noble metal M'noble substrate by the second noble metal M'noble is shown in schematic A. Schematic B shows the adsorption of M<sub>noble</sub>

on a reactive metal M substrate, followed by etching the metal atoms from the substrate side [47].

#### 1.7.5 Electrodeposition:

Electrodeposition is a known procedure for adding metal layers to conductive materials. With one sample and one solvent, the negative part of the cathode holds the sample closed and open and the current through all 34 internal circuits gives the movement speed. Since this method is fast and economical, it supports the creation of detailed and complicated-looking devices. How thick the layer becomes depends only on the present density and the way the current is flowing. Chemically, the envelope can be unblown by changing the substrate into a soluble form [48]. Electronic materials can be covered with a thin conducting layer in an aqueous solution using introduced voltage which induces the required chemical reactions. This approach can be applied to growing metal oxides and chalcogenides in nanostructured materials. Finished films are often built on large, detailed layouts, spanning a size range of only a few nanometers up to ten microns. This variety in size means the process is flexible for many industries.

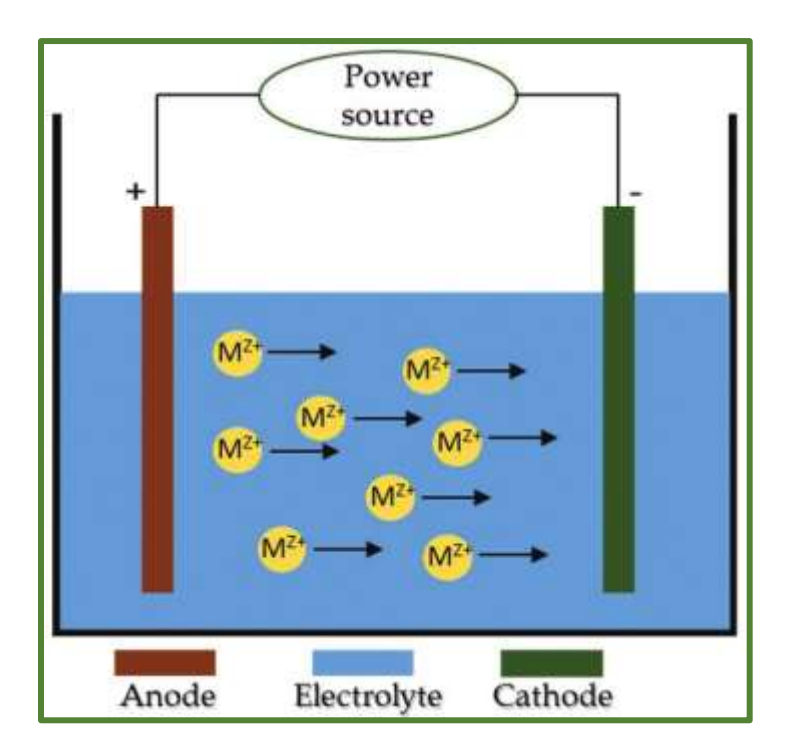


Figure 1.15: Schematic of an electrodeposition process [49].

#### 1.7.6 Dealloying:

Dealloying means removing a particular component or components from a solid solution alloy. Dealloying presents a range of conditions and develops in the form of a porous, sponge-like microstructure. The pores often link together, but small chunks of more valuable materials usually stay separate. Such is the case that dealloyed parts are vulnerable to stress corrosion cracking (SCC). Localized porous structures generated during dealloying are usually found at pre-existing cracks. External stress may then trigger fracture in the corroded material and make the crack move into the surrounding, uncorroded part. Many models have been developed to explain how dealloying corrosion takes place. The main diffusion models are bulk diffusion, vacancy diffusion, surface diffusion, dissolution and reprecipitation, oxide formation and percolation. Data on corrosion rates shows that the surface diffusion model is the likely mechanism.

Dezincification is found most often in the dealloying corrosion of brass. Brass alloys containing zinc (Cu–Zn) are dissolved selectively when exposed for a long time to solutions that contain chlorides. The joint  $\alpha$  and  $\beta$  phase of these alloys is most at risk, as the majority of attack happens in the zinc-rich  $\beta$  part. As a result of dezincification, there is a porous area of weakened copper and some copper oxide. At room temperature, dezincification happens with slightly acidic water and acid chlorides and the  $\beta$  phase shows a uniform effect. At higher temperatures, the effect is more clearly noticeable in focused areas with very high penetration. Purifying process streams, restricting the zinc content and replacing zinc with better corrosion-resistant materials prevent the problem of dezincification [50].

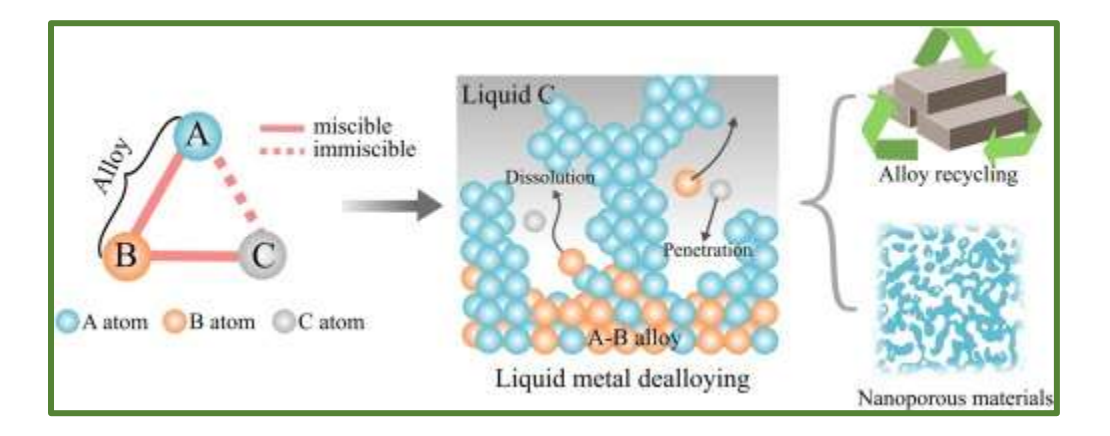


Figure 1.16: A schematic shows the liquid metal dealloying Process [51].

## 1.7.6 Ball milling:

One of the cheapest and most used methods for preparing nanosize metal particles is ball milling, where you use hard steel, ceramic or tungsten balls. A large amount of metal hydrides with the correct properties can be produced in a single step through high-energy mechanical ball milling. Metal hydrides are usually protected with an inert atmosphere in ball milling for safety reasons. Nanosized metal hydrides made by mechanochemistry have different grain shapes, dislocations and surface and internal breaks. According to the Griffith theory (Eq. 1.6), brittle materials consume energy as they form cracks. In ductile materials, it is plastic deformation that means their energy consumption. Ductile materials absorb more energy as they are processable over a plastic region [52].

$$\sigma f \propto \sqrt{\frac{\gamma cE}{a}} \tag{1.7}$$

where  $\sigma_f$  is the applied failure stress,  $\gamma_c$  is the specific surface energy, a is half the crack length, and E is Young's modulus.

#### **References:**

- [1] Latturner, Susan E. "From Ternary to Quaternary Rare Earth Carbide Intermetallics: Trends in Structural Characteristics." *Deleted Journal*, 2024, pp. 275–319. <a href="https://doi.org/10.1016/bs.hpcre.2024.05.001">https://doi.org/10.1016/bs.hpcre.2024.05.001</a>.
- [2] Mitra, Rahul. Structural Intermetallics and Intermetallic Matrix Composites. 2015, https://doi.org/10.1201/b18434.
- [3] Balasubramanian, Karthik, et al. "Valence Electron Concentration as an Indicator for Mechanical Properties in Rocksalt Structure Nitrides, Carbides and Carbonitrides." *Acta Materialia*, vol. 152, Apr. 2018, pp. 175–85. https://doi.org/10.1016/j.actamat.2018.04.033.
- [4] <u>Jürgen Nuss</u> and al, "Intermetallic phases." *Max Planck Institute for Solid State Research*, www.fkf.mpg.de/86707/Intermetallic Phases.
- [5] Stein, F., Leineweber, A. Laves phases: a review of their functional and structural applications and an improved fundamental understanding of stability and properties. *J Mater Sci* **56**, 5321–5427 (2021). <a href="https://doi.org/10.1007/s10853-020-05509-2">https://doi.org/10.1007/s10853-020-05509-2</a>.
- [6] Schulze GER (1939) Zur Kristallchemie der intermetallischen AB2-Verbindungen (Laves-Phasen) (About the crystal chemistry of the intermetallic AB2 compounds (Laves phases); in German). Z Elektrochem 45:849–865. <a href="https://doi.org/10.1002/bbpc.19390451202">https://doi.org/10.1002/bbpc.19390451202</a>.
- [7] Murty, B. S., et al. "Intermetallics, Interstitial Compounds and Metallic Glasses in High-Entropy Alloys." *Elsevier eBooks*, 2014, pp. 119–31. <a href="https://doi.org/10.1016/b978-0-12-800251-3.00007-9">https://doi.org/10.1016/b978-0-12-800251-3.00007-9</a>.
- [9] Heusler, Otto. « Kristallstruktur Und Ferromagnetismus Der Mangan-Aluminium-Kupferlegierungen ». Annalen Der Physik, vol. 411, n° 2, janvier 1934, p. 155-201. DOI.org (Crossref), <a href="https://doi.org/10.1002/andp.19344110205">https://doi.org/10.1002/andp.19344110205</a>.
- [10] Sheron Tavares, Kesong Yang, Marc A. Meyers, Heusler alloys: Past, properties, new alloys, and prospects, Progress in Materials Science, Volume 132, 2023, 101017, ISSN 0079-6425, <a href="https://doi.org/10.1016/j.pmatsci.2022.101017">https://doi.org/10.1016/j.pmatsci.2022.101017</a>.

- [13] Planes, Antoni, et al. "Magnetocaloric Effect and Its Relation to Shape-memory Properties in Ferromagnetic Heusler Alloys." *Journal of Physics Condensed Matter*, vol. 21, no. 23, May 2009, p. 233201. https://doi.org/10.1088/0953-8984/21/23/233201.
- [14] Entel, P., Gruner, M. E., Acet, M., Çakır, A., Arróyave, R., Duong, T., Sahoo, S., Fähler, S., & Sokolovskiy, V. V. (2018). Properties and Decomposition of Heusler Alloys. *Energy Technology*, 6(8), 1478–1490. <a href="https://doi.org/10.1002/ente.201800256">https://doi.org/10.1002/ente.201800256</a>.
- [16] Jeitschko, W. "Transition Metal Stannides with MgAgAs and MnCu2Al Type Structure." *Metallurgical Transactions*, vol. 1, no. 11, Nov. 1970, pp. 3159–62. <a href="https://doi.org/10.1007/bf03038432">https://doi.org/10.1007/bf03038432</a>
- [17] Zhang, Qingdong, et al. "Mechanical Properties of DO3 Based on First Principles." *Crystals*, vol. 10, no. 6, June 2020, p. 488. https://doi.org/10.3390/cryst10060488.
- [18] Liu, Hao, et al. "Bulk and Surface Half-metallicity: The Case of D03-type Mn3Ge." Journal of Applied Physics, vol. 115, no. 3, Jan. 2014, <a href="https://doi.org/10.1063/1.4861875">https://doi.org/10.1063/1.4861875</a>.
- [20] Graf, Tanja, et al. "Crystal Structure of New Heusler Compounds." *Zeitschrift Für Anorganische Und Allgemeine Chemie*, vol. 635, no. 6–7, Mar. 2009, pp. 976–81. https://doi.org/10.1002/zaac.200900036.
- [22] O. Baraka, S. Malki, L. El farh, A. Yakoubi, D. Sébilleau, First-principles calculations of structural, magneto-electronic, mechanical, optical and thermoelectric properties of novel quaternary Heusler alloys type ZrCoYAs (Y= Fe and Mn), Solid State Communications, Volume 392, 2024, 115651, JSSN 0038-1098, https://doi.org/10.1016/j.ssc.2024.115651.
- [23] Bainsla, Lakhan, and K. G. Suresh. "Equiatomic Quaternary Heusler Alloys: A Material Perspective for Spintronic Applications." *Applied Physics Reviews*, vol. 3, no. 3, July 2016, p. 031101. <a href="https://doi.org/10.1063/1.4959093">https://doi.org/10.1063/1.4959093</a>.
- [25] Schäfer, Herbert. "On The Problem of Polar Intermetallic Compounds: The Stimulation of E. Zintl's Work for the Modern Chemistry of Intermetallics." *Annual Review of Materials Science*, vol. 15, no. 1, Aug. 1985, pp. 1–42. https://doi.org/10.1146/annurev.ms.15.080185.000245.
- [26] Schäfer, H. "Semimetal Clustering in Intermetallic Phases." *Journal of Solid-State Chemistry*, vol. 57, no. 1, Mar. 1985, pp. 97–111. <a href="https://doi.org/10.1016/s0022-4596(85)80063-3">https://doi.org/10.1016/s0022-4596(85)80063-3</a>.

- [28] Janka, O., & Kauzlarich, S. M. (2004). Zintl Compounds. *Encyclopedia of Inorganic and Bioinorganic Chemistry*, 1–14. https://doi.org/10.1002/9781119951438.eibc0244.pub2
- [29] Hume-Rothery, W. Researches on the nature, properties, and conditions of formation of intermetallic compounds, with special reference to certain compounds of tin-I-V. *J. Inst. Met.* **1926**, *35*, 295–361.
- [30] Mizutani U, Sato H. The Physics of the Hume-Rothery Electron Concentration Rule. Crystals. 2017; 7(1):9. <a href="https://doi.org/10.3390/cryst7010009">https://doi.org/10.3390/cryst7010009</a>
- [31] Mott, N.F.; Jones, H. *The Theory of the Properties of Metals and Alloys*; Clarendon Press: Oxford, UK, 1936; Dover Publications Inc.: New York, NY, USA, 1958.
- [32] Raynor, G. (1949). Progress in the theory of alloys. *Progress in Metal Physics*, *1*, 1–76. https://doi.org/10.1016/0502-8205(49)90003-9.
- [33] Bain, Gordon A., and John F. Berry. "Diamagnetic Corrections and Pascal's Constants." *Journal of Chemical Education*, vol. 85, no. 4, Apr. 2008, p. 532. <a href="https://doi.org/10.1021/ed085p532">https://doi.org/10.1021/ed085p532</a>.
- [34] I. R. Muts, V. I. Zaremba, U. Ch. Rodewald, W. Hermes, R. Pöttgen, Z. Anorg. Allg. Chem. 2007, 633, 2725.
- [35] Zh. Wu, H. Eckert, J. Senker, D. Johrendt, G. Kotzyba, B. D. Mosel, H. Trill, R.-D. Hoffmann, R. Pöttgen, J. Phys. Chem. B 2003, 107, 1943.
- [36] Bardeen, J., Cooper, L. N., & Schrieffer, J. R. (1957). Theory of Superconductivity. *Physical Review*, *108*(5), 1175–1204. <a href="https://doi.org/10.1103/physrev.108.1175">https://doi.org/10.1103/physrev.108.1175</a>.
- [38] Kamihara, Yoichi, et al. "Iron-Based Layered Superconductor: LaOFeP." Journal of the American Chemical Society, vol. 128, no. 31, July 2006, pp. 10012–13. https://doi.org/10.1021/ja063355c.
- [39] Kamihara, Yoichi, Takumi Watanabe, et al. "Iron-Based Layered Superconductor La[O1-xFx] FeAs (X = 0.05-0.12) With Tc = 26 K." *Journal of the American Chemical Society*, vol. 130, no. 11, Feb. 2008, pp. 3296–97. https://doi.org/10.1021/ja800073m .
- [40] DiSalvo, Francis J. "Thermoelectric Cooling and Power Generation." *Science*, vol. 285, no. 5428, July 1999, pp. 703–06. <a href="https://doi.org/10.1126/science.285.5428.703">https://doi.org/10.1126/science.285.5428.703</a>.

- [41] Carlini, R., Marré, D., Pallecchi, I., Ricciardi, R., & Zanicchi, G. (2013). Thermoelectric properties of Zn4Sb3 intermetallic compound doped with Aluminum and Silver. *Intermetallics*, 45, 60–64. <a href="https://doi.org/10.1016/j.intermet.2013.10.002">https://doi.org/10.1016/j.intermet.2013.10.002</a>.
- [42] R. A. Huggins, Lithium alloys electrodes, in: J. O. Besenhard (Ed.), Handbook of battery materials, Part III, Chapter 4, Wiley-VCH, Weinheim, 1999.
- [43] Hou, Zhiquan, et al. "Exploring Intermetallic Compounds: Properties and Applications in Catalysis." *Catalysts*, vol. 14, no. 8, Aug. 2024, p. 538. <a href="https://doi.org/10.3390/catal14080538">https://doi.org/10.3390/catal14080538</a>.
- [44] Meher, Arabinda, et al. "A Review on Manufacturability of Magnesium Matrix Composites: Processing, Tribology, Joining, and Machining." CIRP Journal of Manufacturing Science and Technology, vol. 39, Aug. 2022, pp. 134–58. https://doi.org/10.1016/j.cirpj.2022.07.012.
- [46] Cheng, Haoyan, et al. "Galvanic Replacement Synthesis of Metal Nanostructures: Bridging the Gap Between Chemical and Electrochemical Approaches." Accounts of Chemical Research, vol. 56, no. 7, Mar. 2023, pp. 900–09. <a href="https://doi.org/10.1021/acs.accounts.3c00067">https://doi.org/10.1021/acs.accounts.3c00067</a>.
- [48] Jasni, Ainil Hawa. "Fabrication of Nanostructures by Physical Techniques." Elsevier eBooks, 2021, pp. 131–62. https://doi.org/10.1016/b978-0-12-820569-3.00005-0.
- [50] W.F. Gale, T.C. Totemeier, editor. "Corrosion." Elsevier eBooks, 2004, pp. 31–13. https://doi.org/10.1016/b978-075067509-3/50034-8.
- [52] Desai, Fenil J., et al. "A Critical Review on Improving Hydrogen Storage Properties of Metal Hydride via Nano structuring and Integrating Carbonaceous Materials." *International Journal of Hydrogen Energy*, vol. 48, no. 75, Apr. 2023, pp. 29256–94. <a href="https://doi.org/10.1016/j.ijhydene.2023.04.029">https://doi.org/10.1016/j.ijhydene.2023.04.029</a>.

#### **Figures:**

- [8] Wang, D., Van Der Wee, E. B., Zanaga, D., Altantzis, T., Wu, Y., Dasgupta, T., Dijkstra, M., Murray, C. B., Bals, S., & Van Blaaderen, A. (2021). Quantitative 3D real-space analysis of Laves phase supraparticles. *Nature Communications*, *12*(1). <a href="https://doi.org/10.1038/s41467-021-24227-0">https://doi.org/10.1038/s41467-021-24227-0</a>.
- [11] Alexander & P. Poudeu, Pierre & Uher, Ctirad. (2016). A first-principles approach to half-Heusler thermoelectrics: Accelerated prediction and understanding of material properties. Journal of Materiomics. 2. https://doi.org/10.1016/j.jmat.2016.04.006.
- [12] Wederni, A.; Daza, J.; Ben Mbarek, W.; Saurina, J.; Escoda, L.; Suñol, J.-J. Crystal Structure and Properties of Heusler Alloys: A Comprehensive Review. Metals 2024, 14, 688. <a href="https://doi.org/10.3390/met14060688">https://doi.org/10.3390/met14060688</a>.
- [15] Tavares, Sheron, et al. "Heusler Alloys: Past, Properties, New Alloys, and Prospects." Progress in Materials Science, vol. 132, Sept. 2022, p. 101017. <a href="https://doi.org/10.1016/j.pmatsci.2022.101017">https://doi.org/10.1016/j.pmatsci.2022.101017</a>.
- [19] Wederni, Asma, et al. "Crystal Structure and Properties of Heusler Alloys: A Comprehensive Review." *Metals*, vol. 14, no. 6, June 2024, p. 688. <a href="https://doi.org/10.3390/met14060688">https://doi.org/10.3390/met14060688</a>.
- [21] Životský O, Skotnicová K, Čegan T, Juřica J, Gembalová L, Zažímal F, Szurman I. Structural and Magnetic Properties of Inverse-Heusler Mn<sub>2</sub>FeSi Alloy Powder Prepared by Ball Milling. *Materials*. 2022; 15(3):697. <a href="https://doi.org/10.3390/ma15030697">https://doi.org/10.3390/ma15030697</a>.
- [24] Winter, G., Matzelle, M., Lane, C., & Bansil, A. (2020c, November 3). Fully-Compensated Ferrimagnetic Spin Filter Materials within the CrMNAl Equiatomic Quaternary Heusler Alloys. Retrieved from <a href="https://arxiv.org/abs/2011.01389">https://arxiv.org/abs/2011.01389</a>.
- [27] Janka, Oliver & Kauzlarich, Susan. (2004). Zintl Compounds. 10.1002/9781119951438.eibc0244.pub2.
- [37] Pöttgen, R. (2019a). Preface of the Second Edition. In De Gruyter eBooks (p. V–VI). <a href="https://doi.org/10.1515/9783110636727-201">https://doi.org/10.1515/9783110636727-201</a>.

- [45] Majid, Abdul, and Maryam Bibi. "Wet Chemical Synthesis Methods." *Topics in mining, metallurgy and materials engineering*, 2017, pp. 43–101. https://doi.org/10.1007/978-3-319-68753-7 3.
- [46] Papadakis, Athanasios, et al. "Electrocatalysts Prepared by Galvanic Replacement." *Catalysts*, vol. 7, no. 3, Mar. 2017, p. 80. https://doi.org/10.3390/catal7030080.
- [49] Mundotiya, Brij Mohan, and Wahdat Ullah. "Morphology Controlled Synthesis of the Nanostructured Gold by Electrodeposition Techniques." *IntechOpen eBooks*, 2019, https://doi.org/10.5772/intechopen.80846.
- [51] Guo, Xueyi, et al. "Liquid Metals Dealloying as a General Approach for the Selective Extraction of Metals and the Fabrication of Nanoporous Metals: A Review." *Materials Today Communications*, vol. 26, Jan. 2021, p. 102007. <a href="https://doi.org/10.1016/j.mtcomm.2020.102007">https://doi.org/10.1016/j.mtcomm.2020.102007</a>.

# CHAPTER II:

Electronic structure theory and Wien2k Code

#### 2.1 Introduction:

By utilizing solid-state physics and applying quantum mechanics to molecular systems, we can derive a range of physical and chemical properties, including structural, optical, elastic, electronic, and magnetic characteristics. Quantum mechanics started taking form in the early part of the 20th century, starting with Max Planck's discovery of blackbody radiation quantization in 1905 [1] and Albert Einstein's explanation of the photoelectric effect [2]. These advances laid the foundation for Niels Bohr's atomic model in 1913 [3], which revolutionized atomic theory by incorporating Planck and Einstein's energy quantization principles.

Every physical object demonstrates dual entities of wave and particle characteristics through wave-particle duality. became more defined and led to a broader understanding of quantum phenomena. The discovery stands as one of the major transformative events in 20th century science since it transformed our perception of physics. Building on these developments, Erwin Schrödinger [4] formulated the wave equation that defines modern quantum mechanics, describing the motion of electrons and atoms through the equation:

$$H\psi = \epsilon\psi \tag{2.1}$$

The equation expresses H as Hamiltonian operator while  $\psi$  represents wave function and  $\epsilon$  indicates system's total energy. The exact solution of Schrödinger's equation applies only to lone-electron systems so researchers need approximate solutions to model systems with multiple electrons. This chapter covers basic quantum mechanics concepts, introduces approximations for solving Schrödinger's equation, and discusses the Hohenberg-Kohn theorems, which form the basis of DFT by using electron density instead of the wave function. It also explains the exchange-correlation term and explores solving DFT equations using a plane wave basis.

# 2.2 Solving Schrödinger's equation for a crystalline solid:

The physical properties of a solid stem from the behavior of its electronic structure. This concerns the movement of light electrons around heavy nuclei, for which quantum theory provides the perfect framework. In a quantum system with n electrons and N nuclei, congruent wave

functions are necessary. In principle, the time-independent Schrodinger equation provides a way to obtain these values.

$$\widehat{H}\psi(\vec{r}_i,\vec{R}_I) = \epsilon\psi(\vec{r}_i,\vec{R}_I) \tag{2.2}$$

Both  $\vec{r}_i$  and  $\vec{R}_I$  represent the coordinates position of the electrons and nuclei, respectively. The non-relativistic Hamiltonian  $\hat{H}$  originates entirely from electrostatic interactions between electron-electron as well as electron-nucleus and nucleus-nucleus forces together with kinetic energies.

$$\widehat{H} = -\frac{1}{2} \sum_{i=1}^{n} \vec{V}_{i}^{2} - \frac{1}{2} \sum_{l=1}^{N} \vec{V}_{l}^{2} - \sum_{l=1}^{N} \sum_{i=1}^{n} \frac{z_{l}}{|\vec{r}_{i} - \vec{R}_{l}|} + \frac{1}{2} \sum_{i \neq j}^{n} \frac{1}{|\vec{r}_{i} - \vec{r}_{j}|} + \frac{1}{2} \sum_{l \neq j}^{N} \frac{1}{|\vec{R}_{l} - \vec{R}_{l}|}$$
(2.3)

Or in short form:

$$\widehat{H} = T_n + T_e + U_{e-n} + U_{e-e} + U_{n-n}$$
(2.4)

- $T_n$ : The kinetic energy of the nuclei.
- $T_e$ : The kinetic energy of the electrons.
- $U_{n-n}$ : The potential energy of interaction between the nuclei.
- $U_{e-n}$ : The potential energy of attraction between nuclei and electrons.
- $U_{e-e}$ : The potential energy of repulsion between electrons.

# 2.2.3 The Born-Oppenheimer approximation:

According to Born and Oppenheimer [5] the fast-moving and light electrons surpass the slow-moving heavy nuclear masses so the nuclear motions can be neglected through the adiabatic approximation. The elimination of nuclear kinetic energy makes nucleus-nucleus potential energy into a constant that serves as the new energy origin. The Hamiltonian then becomes:

$$\widehat{H} = T_e + U_{e-n} + U_{e-e} \tag{2.5}$$

Under the adiabatic approximation of the Schrödinger equation the system wave function takes the expression

$$\psi(\vec{r}_i, \vec{R}_I) = \psi_e(\vec{r}_i)\psi_n(\vec{R}_i) \tag{2.6}$$

Where:

- $\psi_n(\vec{R}_i)$ : nuclear wave function.
- $\psi_e(\vec{r}_i)$ : electronic wave function.

There are several methods to solve equation (2.2), with the first being the free-electron hypothesis introduced by Hartree and Hartree-Fock [6-7].

## 2.2.4 Hartree approximation:

The basic idea of this approximation relies on the assumption that the electrons move independently of one another (i.e., without bonding or spin interactions), All electrons in the system belong to a mean field that includes the combined presence of other electrons together with nuclear elements. Thus, when observing two electrons, 1 and 2, the appearance of electron 1 with coordinates  $r_1$  in orbital 1 is independent of the presence of electron 2 with coordinates  $r_2$ . The Hamiltonian of such a system is expressed as:

$$H = \sum_{i=1}^{N} h(i) \tag{2.7}$$

h(i): single-electron Hamiltonian.

When this happens the wave function of n electrons divides into separate wave functions that describe each electron.

$$\psi(\vec{r}) = \sum_{i=1}^{n} \psi_i(\vec{r}) \tag{2.8}$$

The Schrödinger equation for n electrons becomes n single-electron Schrödinger equations:

$$\left[ -\frac{1}{2}\nabla_i^2 + U_{ext}(\vec{r}_i, \vec{R}) + U_H(\vec{r}_i, \vec{r}_j) \right] \psi_i(\vec{r}) = \epsilon_i \psi_i(\vec{r})$$
 (2.9)

 $U_{ext}(\vec{r_i}, \vec{R})$ : The interaction between the electron  $\vec{r_i}$  and the nuclei with coordinates  $\vec{R}$ .

 $U_H(\vec{r}_i, \vec{r}_j)$ : The Hartree potential arises from the interaction between the electron with coordinates  $\vec{r}_i$  and the mean field of the additional electrons at coordinates  $\vec{r}_j$ .

#### 2.2.5 Hartree-Fock approximation (1930):

To further simplify the Hamiltonian, the Hartree approximation [6] treats electrons as indistinguishable particles. Since electrons are fermions (spin 1/2), Pauli's exclusion principle ensures that no two electrons can occupy the same quantum state. The Hartree-Fock approximation in reference [7] develops Hartree's method by requiring wave function symmetry which produces exchange interactions. The exchange interaction emerges because of Pauli's exclusion principle that derives from Heisenberg's principle demonstrating that wave functions for a given system need antisymmetric when two particles are exchanged. Fock present the wave function for nelectron systems through linear compositions of independent electron wave functions arranged as Slater determinants [8].

$$\psi(\vec{r}_{1}, \vec{r}_{2}, ..., \vec{r}_{n},) = \frac{1}{\sqrt{n!}} \begin{bmatrix} \psi_{1}(\vec{r}_{1}) & \psi_{2}(\vec{r}_{1}) ... & \psi_{n}(\vec{r}_{1}) \\ \psi_{1}(\vec{r}_{2}) & \psi_{2}(\vec{r}_{2}) ... & \psi_{n}(\vec{r}_{2}) \\ \vdots & \vdots & \vdots \\ \psi_{1}(\vec{r}_{n}) & \psi_{2}(\vec{r}_{n}) ... & \psi_{n}(\vec{r}_{n}) \end{bmatrix}$$
(2.10)

 $\psi$  The wave function  $\psi$  represents a system containing n electrons that exists within the spin-orbit representation. When electrons are exchanged in position between two elements this results in two rows of the determinant (equation 2.10) being swapped leading to a sign change in  $\psi$ . The two electrons share the same spin-orbit state according to the Pauli-Heisenberg principle as their wave functions cannot occupy the same state.

The exchange term defines the sole distinction between Hartree and Hartree-Fock computational approaches. Each orbital suffers electrostatic mean field treatment in the Hartree-Fock approach as the exchange operator represents the energetic changes resulting from electrons having parallel spins occupying identical positions.

# 2.3 Density functional theory DFT:

Real quantum mechanical systems resist direct solution of the Schrödinger equation because of their excessive number of interactions. To tackle this challenge, one replaces the wave function functional with a density functional, a technique called density functional theory (DFT). We consider the qualification because it describes systems by using electronic density as the main variable for a straightforward evaluation of electronic electronegative interactions.

The initial ideas in this direction were pioneered by Thomas and Fermi in 1927 with their electronic density model. But, DFT as we know it today was formalized by the groundbreaking work of Hohenberg and Kohn who put forward two fundamental theorems. These theorems say that all properties of a system depend only on its electronic density and that a universal energy functional exists which can determine this density in a certain ground state. These principles formed the basis of modern DFT that has grown into an essential component of theoretical physics and chemistry.

#### 2.3.1 The two theorems of Hohenberg and Kohn:

Hohenberg and Kohn established DFT theory formally in 1964 by publishing two proof-based theorems in their recognized papers [11].

# 2.3.1.A First Hohenberg-Kohn theorem:

Hohenberg and Kohn presented in their first segment that the ground-state electronic density serves as a complete functional representation to describe the external potential. Hence, all observables associated with this state are functionals of the external potential. Thus, energy functional is defined as:

$$\mathbf{E} = \mathbf{E}(\mathbf{\rho}) \tag{2.11}$$

The simplification of the Schrödinger equation is one of the biggest advantages of DFT methods. It just depends on the measurable  $\rho$  which is set in the physical space  $R^3$  Rather than on the 3N dimensional configuration space. once the chemical potential is determined from the density  $\rho$  ( $\vec{r}$ ) all electronic properties will become obtainable. It has a kinetic component; The potential generates this quantity which functions as a functionally unique operator of the density. This is the underlying result of DFT. The energy is now an implicit functional due to the exchange-correlation

energy  $E_{XC}(\vec{r})$  If the external potential changes, the density will change also. This  $E_{XC}(\vec{r})$  is composed of:

- The kinetic energy excess compared to the one of a non-interacting electron gas.
- The interaction energy (actual minus Hartree, while including all the multi-body contributions.

One of the main points encapsulated in the first theorem is that the total energy and consequently all physical properties derived from it are basis independent when it comes to the wave function used to build the density.

#### 2.3.1.B Second Hohenberg-Kohn theorem:

The theorem establishes that the minimum energy ground state density represents the actual density while other ground state characteristics depend on this density. The theorem states:

$$E(\rho_0) = minE(\rho) \tag{2.12}$$

The functional for the total ground state energy takes the following form:

$$E[\rho(\vec{r})] = F[\rho(\vec{r})] + \int \hat{V}_{ext} (\vec{r}) \rho(\vec{r}) d^3 r^3$$
 (2.13)

Where:

- $\hat{V}_{ext}$  is the external potential acting on the particles.
- $F[\rho(\vec{r})]$  is the universal functional by Hohenberg and Kohn, defined as:

$$F[\boldsymbol{\rho}(\vec{r})] = \langle \Psi | \hat{T} + \hat{V} | \Psi \rangle \tag{2.14}$$

The idea behind this function is to increase the overall energy and charge density of the fundamental state for an agreed-upon external potential.

# 2.3.2 Kohn-Sham equations (orbital approach):

The Hohenberg-Kohn theorem stands as a theoretical basis which enables solving the Schrödinger equation by using electronic density as its primary variable. The ground state energy calculation proceeds through an iterative process based on variational principles due to the fact that NNN interacting electron systems have their energy defined by a functional of density.

A new functional named F [ $\rho$  ( $r^{-}$ )] was introduced since it ignores specific details about electronic systems to compute their total energy. The functional which has been mentioned previously consists of two terms:  $T_{el}$  that represents electron kinetic energy and  $V_{el-el}$  representing electron interactive energy. which are both functionals of the density. Yet, their explicit analytical expressions for a N interacting electron system i.e., N interacting electrons are yet unknown.

The issue was addressed from a different angle by Kohn and Sham [12]. Similar to the known expression of the classical potential energy (Hartree energy) they understood that getting an accurate term for kinetic energy is crucial just as important. To establish this method, they created a fictitious model with non-interacting electrons which possessed equal density  $\rho$  ( $r^{\rightarrow}$ ) as the interacting system:

$$\rho(r) = \sum_{i}^{occ} \Psi_{l}(r) \Psi_{i}^{*}(r)$$
(2.15)

The sum is carried out on occupied states.

Note that the electronic density  $\rho(\vec{r})$  is a positive function of three three-dimensional coordinates. It disappears at infinity  $\lim_{r\to\infty}\rho(\vec{r})=0$ , and participates to the total number of electrons N in the whole space.

This makes the energy of the system in the ground state a functional of  $\rho(\vec{r})$ , which reads as the minimum of the following auxiliary functional:

$$E[\rho(r)] = T[\rho(r)] + E_H[\rho(r)] + Exc[\rho(r)] + \int V(r) \rho(r) d^3r$$
 (2.16)

Wherever:

 $T[\rho(\vec{r})]$  is expressed by the following equation which it's the kinetic energy:

$$T[\rho(r)] = -\frac{1}{2} \sum_{i}^{occ} \int d^{3} \Psi_{i}(r) \nabla^{2} \Psi_{i}^{*}(r)$$
 (2.17)

 $E_H$ : The Hartree energy (Coulomb interaction of charge density distributions in the ground state) is given by the following equation:

$$E_{H}[\rho(r)] = \frac{1}{2} \int \frac{\rho(r')\rho(r)}{|r'-r|} d^{3}r'd3$$
 (2.18)

 $E_{XC}$ : The exchange and correlation energy it given by the next equation:

$$E_{xc}[\rho(r)] = \int \varepsilon_{xc} \left[\rho(r)\right] \rho(r) d^3r \qquad (2.19)$$

Solving the ground state requires us to find a self-consistent solution to the Kohn-Sham eigenvalue system.

$$\left[ -\frac{1}{2}\nabla^2 + V_{ext}(r) + V_H(r) + V_{xc}(r) \right] \Psi_i(r) = \varepsilon_i \Psi_i(r)$$
 (2.20)

$$V_H(r) = \frac{\delta E_H}{\delta \rho(r)} = \int d^3 r' \frac{\rho(r')}{r - r'}$$
 (2.21)

$$V_{xc}(\mathbf{r}) = \frac{\delta E_{xc}}{\delta \rho(\mathbf{r})} \tag{2.22}$$

$$V_{ext} = \frac{\partial E_{ext}}{\partial \rho(r)} \tag{2.23}$$

 $\varepsilon_i$ : Represents the eigenenergy associated with the orbital  $\Psi_I$ .

The Kohn-Sham orbitals are provided by solving the Kohn-Sham equation.

$$V_{eff}(r) = V_{eff}(\rho(r)) = V_{eff}(r) + \int d^3 r' \frac{\rho(r')}{|r-r'|} V_{xc}(\rho(r))$$
 (2.24)

Kinetic energy is calculated through a setup of independent electrons moving in a powerful  $V_{eff}(r)$  field that matches the density of real electrons in nuclear-formed areas. Determining the exchange and correlation term stays as the main unresolved issue in this approach. The exchange-correlation part makes up only a small percentage of total energy compared to the electron kinetic energy.

# 2.3.3 Exchange rate processing and correlation:

The theory of density function used within the framework of Kohn-Sham's orbital approach remains exact in its formalization. The indefinite part of the function  $E[\rho]$  gradually gave way to the universal function  $F[\rho]$  and, finally, to the exchange and correlation energy  $E_{XC}[\rho]$ . We need

to analyze the method to define the exchange and correlation function with its set of approximate values.

#### 2.3.3.A Local density approximation (LDA):

In certain model systems, such as the uniform electron gas (which approximates the conduction band electrons in a metal quite well), exact or very highly accurate expressions for the exchange and correlation terms exist. In this Local Density Approximation (LDA) [13], we assume that the electronic density is locally uniform and the exchange-correlation functional is assumed by the following functional form:

$$E_{XC}^{LDA}[\rho] = \int \rho(r) \varepsilon_{xc}[\rho(\vec{r})] d\vec{r}$$
 (2.25)

 $\varepsilon_{xc}$ : The exchange and correlation energy of one particle in a homogeneous electron gas of a given density. It can be located as the sum of an exchange and correlation contribution.

The LDA approximation produces correct results in some cases. By adding electron density gradient information, the generalized gradient approximation first appeared.

#### 2.3.3.B Generalized gradient approximation (GGA):

The Generalized Gradient Approximation (GGA) considers exchange-correlation functionals that depend not only on the electronic density at each point but also on its gradient. This results in a general expression of the following form:

$$E_{xc}^{GGA}[\rho(r)] = \int \rho(\vec{r}) \, \varepsilon_{xc}[\rho(\vec{r}), |\nabla \rho(\vec{r})|] d^3 \vec{r}$$
 (2.26)

 $\varepsilon_{xc}[\rho(\vec{r}), |\nabla\rho(\vec{r})|]$ : It denotes the exchange-correlation energy per electron in an interacting electron system.

# 2.3.3.C mBJ approximation:

Tran and Blaha [14] developed a fresh calculation approach for the energy gap that uses modified Becke-Johnson potential. The updated version of the Becke and Johnson [15] functional takes this structure:

$$v_{x,\sigma}^{mbj}(r) = cv_{x,\sigma}^{BR}(r) + (3c - 2)\frac{1}{\pi}\sqrt{\frac{5}{12}}\sqrt{\frac{2t_{\sigma}(r)}{\rho_{\sigma}(r)}}$$
(2.27)

 $\rho_{\sigma} = \sum_{i=1}^{N_{\sigma}} |\Psi_{i,\sigma}|^2 \rightarrow \text{Electron density.}$ 

 $t_0(r) = \frac{1}{2} \sum_{i=1}^{N_\sigma} |\Psi_{i,\sigma}^* \nabla \Psi_{i,\sigma}|^2 \to \text{Kinetic energy density}$ 

$$v_{x,\sigma}^{RB}(r) \frac{1}{b_{\sigma}(r)} \left[ 1 - e^{X_{\sigma}(r)} - \frac{1}{2} X_{\sigma}(r) e^{-X_{\sigma}(r)} \right] \rightarrow \text{The potential of Becke-Roussel}$$

The Becke-Roussel potential is introduced to minimize the Columbian potential

 $X_{\sigma}(r)$  Is solved by a nonlinear equation involving  $\rho_{\sigma;\nabla\rho_{\sigma}}$ , and  $\nabla^2\rho_{\sigma}t_{\sigma}$ .

The function  $\boldsymbol{b}_{\sigma}$  is written as follows:

$$b_{\sigma} = \left[\frac{X_{\sigma}^3 e^{-x_{\sigma}}}{(8\pi\rho_{\sigma})}\right]^{\frac{1}{3}} \tag{2.28}$$

The Becke-Roussel potential presented here is approximately equivalent to the Slater potential used in the Becke and Johnson approach. The primary modification lies in the introduction of the parameter C within the functional's formula. It is worth noting that when C=1, the Becke and Johnson functional is recovered. This parameter is designed to depend linearly on the square root of the average  $\frac{\overline{V_{\sigma}(r)}}{\rho(r)}$ .

The form of C is given by:

$$C = \alpha + \beta \left( \left( \frac{1}{V_{cell}} \int \frac{\vec{\nabla} \rho(r')}{\rho(r')} D^3 r' \right) \right)^{\frac{1}{2}}$$
 (2.29)

 $\alpha$ ,  $\beta$  Are free parameters

 $V_{cell}$ : The volume of the unit cell of the system with  $\alpha = -0.012$  and  $\beta = -1.023bohr^{\frac{1}{2}}$ 

# 2.4 The Full Potential linearized augmented plane wave method (FP-LAPW):

#### 2.4.1 Introduction:

There are two major categories into which DFT methods are organized: all-electron and pseudo-potential based methods. We are using a first category method that goes by FP-LAPW (Full Potential-Linearized Augmented Plane Wave) method. This method is technically an improvement of the augmented plane wave (APW) method proposed by Slater and was developed by Andersen.

# 2.4.2. Augmented plane wave (APW) method:

Slater proposed the APW (Augmented Plane Wave) method in his article [16]. He stated that the solution to the Schrödinger equation is a plane wave for a constant potential and a radial function for a spherical potential. This led to the introduction of the *muffin-tin* (MT) approximation

to describe the crystalline potential. According to this approach, space is divided into two regions, as illustrated in Fig. 2.1.

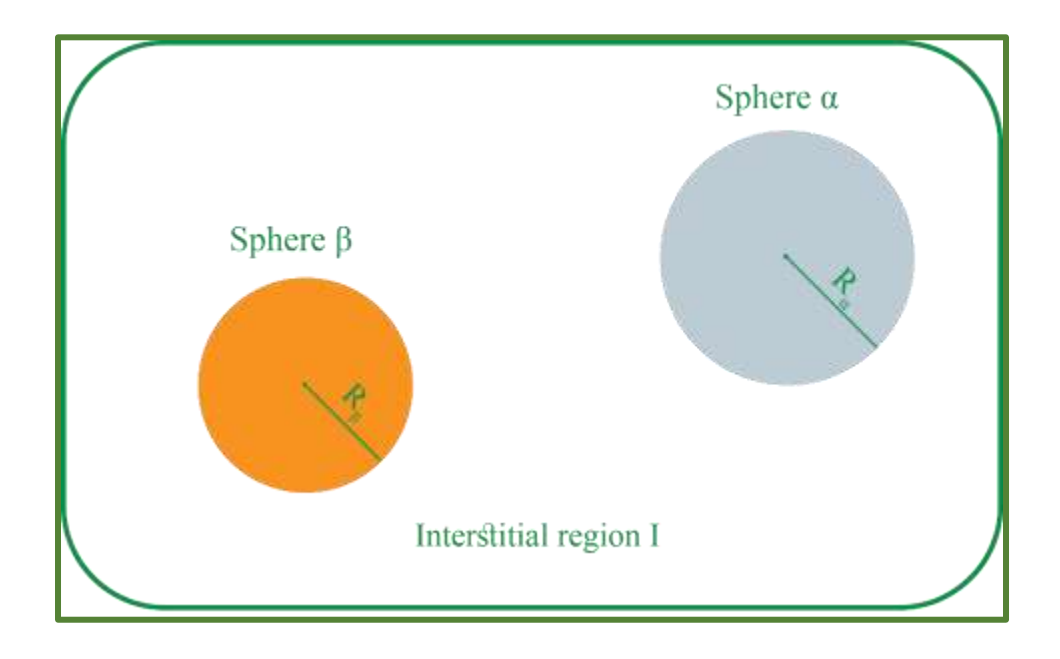


Figure 2.1: Distribution of the unit cell, an interstitial region and spherical regions: α and β spheres of muffin-tin rays and respectively.  $R_{\alpha}R_{\beta}$ 

- 1. a region within muffin tin atomic spheres that surround the nuclei (index  $\alpha$  and  $\beta$ ) and do not overlap.
- 2. the region outside the spheres, called the interstitial region (*I*).

Then, in a region far away from the nuclei (region (I)), electrons are relatively free. But, at proximity to the nuclei (region (S)), their behavior is like that of the electrons surrounding an isolated atom. Thus, one can describe electronic wavefunctions differently in spheres coordinates and in non-spheres coordinates.

So far, we have introduced methods and approximations to compute these wavefunctions based on their development in a specific basis set, the (L) APW (Linearized Augmented Plane Wave).

Here again the choice of this basis set is crucial not only to be sure about the reliability of the results, but also to minimize the computation time necessary.

Therefore, the wavefunction  $\phi(r)$  can be written as [17]:

$$\phi \begin{cases} \frac{1}{\Omega^{1/2}} \sum_{G} C_{G} e^{i(G+K)r} \\ \sum_{lm} A_{lm}(r) U_{l} Y_{lm}(r) \end{cases}$$
 (2.30)

With:

 $R_{\alpha}$ : The radius of the sphere MT.

 $\Omega$ : the volume of the cell

 $C_G \, et \, A_{lm}$ : The coefficients of development in spherical harmonics  $Y_{lm}$ 

The function  $U_l(r)$  is a solution of the Schrödinger equation for the radial part which is written as:

$$\left\{ -\frac{d^2}{dr^2} + \frac{l(l+1)}{r^2} V(r) - E_l \right\} r U_l(r) = 0 \tag{2.31}$$

V(r) is the Muffin-tin potential, and  $E_l$  is the linearization energy. The radial functions are orthogonal to all core eigenstates. But this orthogonality breaks down at the edge of Muffin-tin sphere (MT). In order to make the function  $\phi(r)$  continuous at the surface of the MT sphere, the coefficients  $A_{lm}$  must be expressed in terms of the  $C_G$  coefficients of the plane waves defined in the interstitial regions.

Some algebra shows that:

$$A_{lm} = \frac{4\pi}{\Omega^{\frac{1}{2}}} \frac{i^{l}}{U_{l} r_{l}} \sum_{G} C_{G} J_{l} (|K + G| r_{l}) Y_{lm}^{*} (K + G)$$
 (2.32)

I<sub>1</sub>:Bessel's function

The origin is placed at the center of the sphere, and the coefficients  $A_{lm}$  are determined from the coefficients of the plane waves  $C_G$ , by applying the continuity condition of the wave function  $\phi(r)$  to the surface of the atomic sphere  $\alpha$ . The energy parameters are called the variational coefficients of the APW method.

A more flexible and effective basis to realize the band structure of crystalline lattices is the so-called FP-LAPW method [17-18]. This manner avoids an APW-like division of the space to two distinct areas. In this formalism, we can use more general basis functions in the Muffin-Tin (MT) spheres than in the APW method: they are linear combinations of  $u_l(r)Y_{lm}(r)$  and energy derivatives of  $\dot{u}_l(r)Y_{lm}(r)$ . The key difference with respect to APW, is that the basic functions within the Muffin-Tin (MT) spheres are by themselves linear combinations of radial functions and

their energy derivatives. These functions  $u_l$  are defined as in APW method, but the function  $\dot{u}_l(r)Y_{lm}(r)$  needs to satisfy the following condition:

$$\left\{ -\frac{d^2}{dr^2} + \frac{l(l+1)}{r^2} V(r) - E_l \right\} r U_l(r) = r U_l(r)$$
 (2.33)

In a non-relativistic treatment, the radial functions  $U_l$  and  $\dot{U}_l$  assure continuity with plane waves on the MT sphere's surface. The LAPW method's basic functions are based on the augmented wave functions.

$$\phi(r) = \begin{cases} \frac{1}{\Omega^{1/2}} \sum_{G} C_{G} e^{i(G+K)r} & r > R_{\alpha} \\ \sum_{lm} [A_{lm}(r)U_{l} + B_{lm}U_{l}] Y_{lm}(r) & r < R_{\alpha} \end{cases}$$
(2.34)

Where  $B_{lm}$  are the ones that are accompanied by the function  $\dot{U}_l$ , and  $U_l$  they have the same nature as  $A_{lm}$  coefficients. Like the APW method, the LAPW functions are plane waves only in the interstitial regions. Yet inside spheres, LAPW functions are superior to APW functions. Certainly, when EIE\_l deviates from the band energy E slightly, a linear combination of  $U_l$  and  $\dot{U}_l$  will fit the radial function better than the APW functions a single radial function. It is now possible to treat non-spherical potentials in the Muffin-Tin (MT) spheres without any difficulties.

The FP-LAPW method is an all-electron method (i.e. electron-electron interactions are strong enough, so the contribution of every electron must be considered). Consequently, it is needed a procedure that permits to solve the Kohn-Sham equations without losing the total potential and accounting for the whole set of electrons.

# 2.5 The Wien2k package:

the Wien2k code is a DFT and FP-LAPW based computational code written syntactically in Fortran. Developed by Peter Blaha and Karlheinz Schwarz [19], it was first released in 1990. The C-SHEL script ties together the code, which can be used to run self-consistent calculations with a number of independent programs. So, to start, let's create some input files. Among these, the "case. struct" file is the main input file that describes the structure, including the lattice parameters, atom positions in the unit cell, crystal lattice type, atomic number for each atom, and the space group.

Once the "case. struct". To create the necessary files to carry out a self-consistent field (SCF) calculation, we need to run multiple commands after generating the struct file.

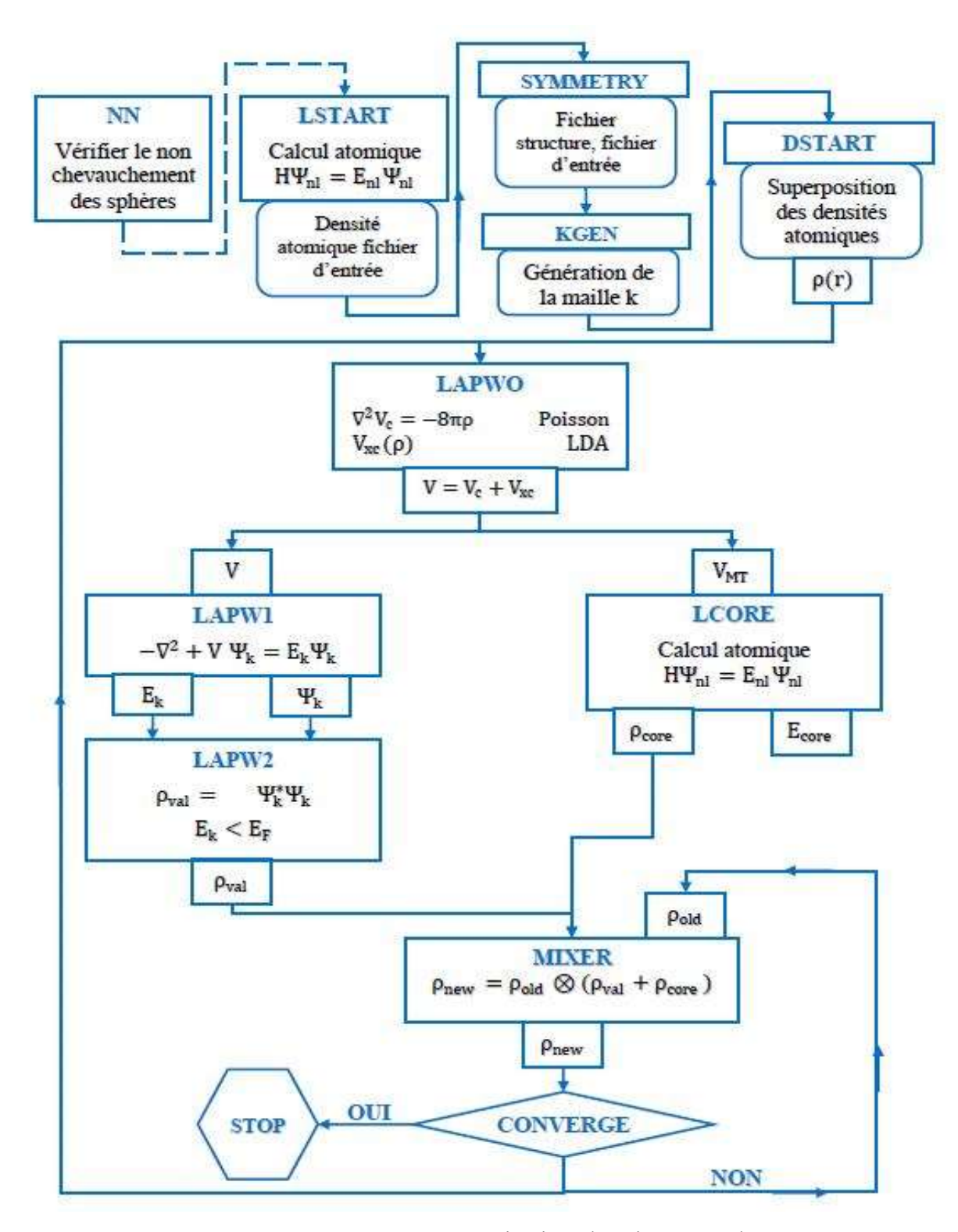


Figure 2.2: Program organization chart in WIEN2k

- NN: This program calculates the distances between the nearest neighbors in a crystal. It helps determine atomic radii and checks for the overlap of the Muffin-Tin spheres, which is crucial for an accurate modeling of the electronic structure.
- **sgroup:** Using the data from the « case.struct » file, this program determines the space group of the crystal and all the point groups of the non-equivalent sites. It then generates a structural file with the appropriate network type, taking into account the symmetries of the system.
- Symmetry: This program generates the symmetry operations of the space group and writes them in the « case.struct\_st » file. Additionally, it determines the point group of each atomic site, which is important for symmetry calculations of electronic wavefunctions.
- kgen: It generates a k-mesh in the Brillouin zone. This mesh is used for sampling wavefunctions in reciprocal space, which is essential for band structure calculations.
- **dstart:** This program generates the initial charge density by superimposing atomic densities generated by the « lstart » program. This provides the first estimate of the electronic density for the self-consistent calculation.
- LAPW0: This program calculates the total potential from the electronic density, taking into account electron-nucleus interactions as well as exchange and correlation effects.
- LAPW1: It constructs the Hamiltonian and calculates the eigenvectors and eigenvalues through diagonalization, thus determining the valence and conduction bands of the system.
- LAPW2: This program calculates the Fermi energy and valence densities, which are necessary for determining the global electronic properties of the system.
- Lapwdm: This program calculates the density matrix necessary for generating orbitals in the charge density and potential calculation.
- Lcore: It calculates the core states for the spherical part of the potential, which allows handling core effects and the central region of the Muffin-Tin sphere.
- Mixer: The « Mixer » program is responsible for mixing the electronic densities of core, semicore, and valence states to generate the input density for the next iteration. In this process, the input

and output densities are combined, and a convergence criterion is applied to ensure the calculations reach a stable solution.

#### **References:**

- [1] M. Planck, Introduction to Physics, Flammarion (1941). Reprinted in the Champs Collection, 204, Flammarion (1989).
- [2] Bohr, N. "I. on the Constitution of Atoms and Molecules." *The London Edinburgh and Dublin Philosophical Magazine and Journal of Science*, vol. 26, no. 151, July 1913, pp. 1–25. https://doi.org/10.1080/14786441308634955.
- [3] Einstein, A. "Über Einen Die Erzeugung Und Verwandlung des Lichtes Betreffenden Heuristischen Gesichtspunkt [AdP 17, 132 (1905)]." *Annalen Der Physik*, vol. 14, no. S1, Feb. 2005, pp. 164–81. https://doi.org/10.1002/andp.200590004.
- [4] Schrödinger, E. "Quantisierung Als Eigenwertproblem." *Annalen Der Physik*, vol. 384, no. 4, Jan. 1926, pp. 361–76. <a href="https://doi.org/10.1002/andp.19263840404">https://doi.org/10.1002/andp.19263840404</a>.
- [5] Born, M., and R. Oppenheimer. "Zur Quantentheorie Der Molekeln." *Annalen Der Physik*, vol. 389, no. 20, Jan. 1927, pp. 457–84. <a href="https://doi.org/10.1002/andp.19273892002">https://doi.org/10.1002/andp.19273892002</a>.
- [6] Hartree, D. R. "The Wave Mechanics of an Atom With a non-Coulomb Central Field. Part III. Term Values and Intensities in Series in Optical Spectra." *Mathematical Proceedings of the Cambridge Philosophical Society*, vol. 24, no. 3, July 1928, pp. 426–37. https://doi.org/10.1017/s0305004100015954.
- [7] Fock, V. (1930) Naherungsmethode zur Losung des quantenmechanischen Mehrkorperproblems. Zeitschrift für Physik, 61, 126-148. http://dx.doi.org/10.1007/BF01340294
- [8] Slater, J. C. "The Theory of Complex Spectra." *Physical Review*, vol. 34, no. 10, Nov. 1929, pp. 1293–322. <a href="https://doi.org/10.1103/physrev.34.1293">https://doi.org/10.1103/physrev.34.1293</a>.
- [9] Pauli, W. "Über Den Zusammenhang des Abschlusses Der Elektronengruppen Im Atom Mit Der Komplexstruktur Der Spektren." *Zeitschrift Für Physik*, vol. 31, no. 1, Feb. 1925, pp. 765–83. <a href="https://doi.org/10.1007/bf02980631">https://doi.org/10.1007/bf02980631</a>.

- [10] Heisenberg, W. "□Ber Den Anschaulichen Inhalt Der Quantentheoretischen Kinematik Und Mechanik." *The European Physical Journal A*, vol. 43, no. 3–4, Mar. 1927, pp. 172–98. <a href="https://doi.org/10.1007/bf01397280">https://doi.org/10.1007/bf01397280</a>.
- [11] Hohenberg, P., and W. Kohn. "Inhomogeneous Electron Gas." *Physical Review*, vol. 136, no. 3B, Nov. 1964, pp. B864–71. <a href="https://doi.org/10.1103/physrev.136.b864">https://doi.org/10.1103/physrev.136.b864</a>.
- [12] Kohn, W., and L. J. Sham. "Quantum Density Oscillations in an Inhomogeneous Electron Gas." Physical Review, vol. 137, no. 6A, Mar. 1965, pp. A1697–705. <a href="https://doi.org/10.1103/physrev.137.a1697">https://doi.org/10.1103/physrev.137.a1697</a>.
- [13] Chaquin, P. and LCT-UPMC. "Pratique De La Chimie Théorique." *Pratique de la Chimie Théorique*, pp. 1–6. <a href="https://www.lct.jussieu.fr/pagesperso/chaquin/Introduction.pdf">www.lct.jussieu.fr/pagesperso/chaquin/Introduction.pdf</a>.
- [14] Tran, Fabien, and Peter Blaha. "Accurate Band Gaps of Semiconductors and Insulators with a Semilocal Exchange-Correlation Potential." Physical Review Letters, vol. 102, no. 22, June 2009, <a href="https://doi.org/10.1103/physrevlett.102.226401">https://doi.org/10.1103/physrevlett.102.226401</a>.
- [15] Pittalis, S., et al. "Becke-Johnson-type Exchange Potential for Two-dimensional Systems." Physical Review B, vol. 81, no. 11, Mar. 2010, <a href="https://doi.org/10.1103/physrevb.81.115108">https://doi.org/10.1103/physrevb.81.115108</a>.
- [16] Slater, J.C. "Energy Band Calculations by the Augmented Plane Wave Method." Advances in quantum chemistry, 1964, pp. 35–58. https://doi.org/10.1016/s0065-3276(08)60374-3.
- [17] Singh, David J. "Planewaves, Pseudopotentials and the LAPW Method." *Springer eBooks*, 2006, <a href="https://doi.org/10.1007/978-0-387-29684-5">https://doi.org/10.1007/978-0-387-29684-5</a>.
- [18] Loucks, T. L. *AbeBooks*. www.abebooks.co.uk/first-edition/Augmented-Plane-Wave-Method-Guide-Performing/31350934241/bd.
- [19] Blaha, P., et al. "Full-potential, Linearized Augmented Plane Wave Programs for Crystalline Systems." Computer Physics Communications, vol. 59, no. 2, June 1990, pp. 399–415. https://doi.org/10.1016/0010-4655(90)90187-6.

# CHAPTER III:

# Results & Discission

#### 3.1 Introduction:

Rare-earth intermetallic compounds [1] stand out because their magnetic properties heavily depend on their composition as well as their crystallographic features. The magnetic attributes of intermetallic compound DyFe<sub>3</sub>Ni<sub>12</sub> stand out because it consists of Dysprosium (Dy), Iron (Fe) and Nickel (Ni). Dysprosium exhibits distinguished characteristics of having an extensive magnetic moment. The mixture finds its primary application in producing advanced magnets. The magnetic properties of DyFe<sub>3</sub>Ni<sub>12</sub> enhance when ferromagnetic Iron and Nickel elements are included which implies that the material might exhibit intricate magnetic configuration. No work has studied the unique characteristics of mechanical and electronic properties observed in this compound despite reasonable predictions. The research aims to analyze the influence that Dysprosium produces on material attributes. Scientific research explores DyFe<sub>3</sub>Ni<sub>12</sub> potential both as a permanent magnet and for magnetic refrigeration applications and other magnetic purposes [2]. Nickel makes the material more chemically stable and enhances its resistance to oxidation.

#### 3.2 Method of calculation:

Our research uses the Wien2k code that depends on the scientific model of density functional theory (DFT). The exchange correlation energy within the local spin density approach of the density functional theory (DFT-LSDA) serves as its representation [3]. The Von Barth-Hedin (VBH) [4] version specifies the parameters for Local Spin Density Approximation (LSDA) when dealing with systems that require two spin densities  $[p(r)\uparrow$  and  $p(r)\downarrow$ . The parameter defines combined spin density as  $[p(r)\uparrow = p(r)\uparrow + p(r)\downarrow]$ . The calculations ran multiple times until both the distribution of charge density reached ( $10^{-5}$  Ry) and satisfied the convergence standards while showing consistent computational results. The integration of Brillouin zone (BZ) used a k-point mesh consisting of 2000 points throughout the self-consistency rounds. We achieved converged energy with a satisfactory volume curve through RMT settings (Dy=2.2300, Fe=2.1300, Ni=2.1600) and Rmt x KMAX=8 and GMAX=14 (a.u) -1 and lmax=8. Here, lmax represents the highest value of angular momentum while Gmax stands for Fourier expansion of charge density and RMT indicates muffin-tin sphere radius minimum with Kmax as highest Fermi wave vector. The Birch-Murnaghan's [5] equation of state (EOS) enabled researchers to obtain optimized

structures of DyFe<sub>3</sub>Ni<sub>12</sub> at these conditions. The WIEN2k program allowed elastic calculations which utilized the IRelast Package for execution.

#### 3.3 Structural data:

Extending FeNi<sub>3</sub> [6] cubic phase into (2x2x2) supercell followed by deposition of dysprosium (Dy) atoms at select iron (Fe) sites produces the new cubic compound DyFe<sub>3</sub>Ni<sub>12</sub> with Im-3m 229 space group and 90° lattice parameters of  $\alpha = \beta = \gamma$ . The crystalline constructs illustrated in Fig. 3.1 originate from VESTA software programming. Table 3.1 below represents the atomic position.

Compound	Atoms	Wyckoff (position)	Coordinates (x, y, z)
DyFe3Ni12	Dy	2a	(0,0,0)
	Fe	6b	(0,1/2,0)
	Ni	24h	(1/4,1/2,1/4)
FeNi3 [26]	Fe	1a	(0,0,0)
	Ni	3c	(0,1/2,1/2)

Table 3.1: Atomic position of Dysprosium, Nickel, Iron in DyFe<sub>3</sub>Ni<sub>12</sub> and FeNi<sub>3</sub>

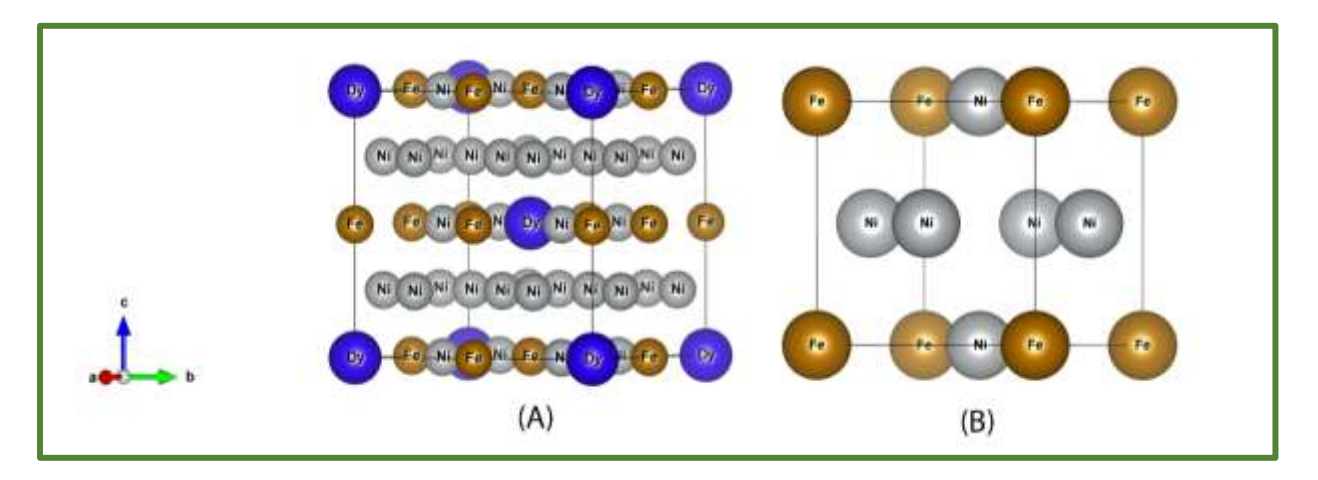
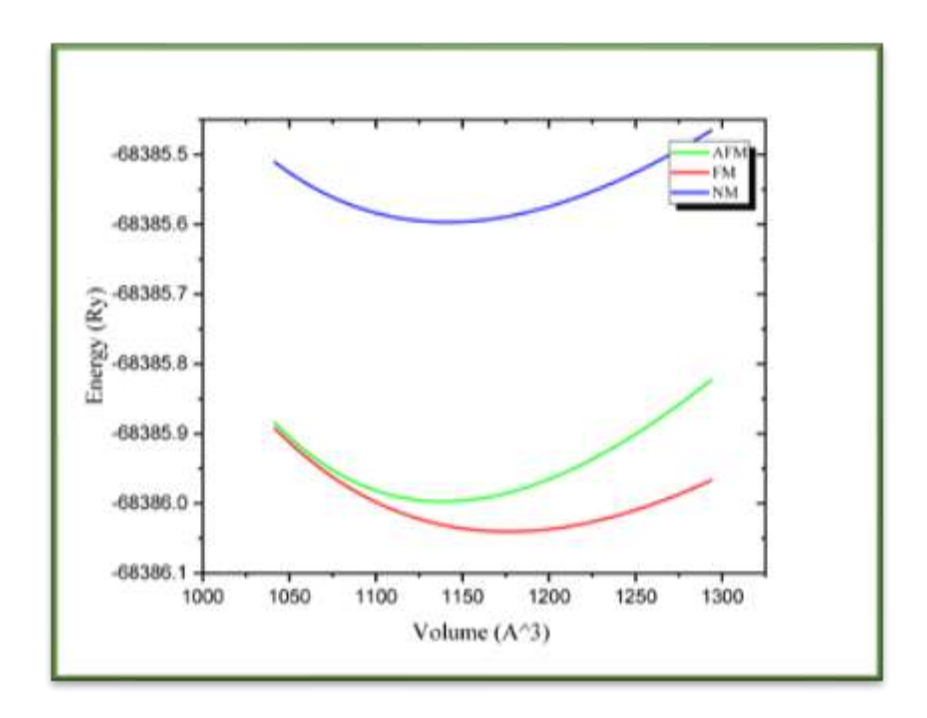


Figure 3.1: (A) The atomic structure of DyFe<sub>3</sub>Ni<sub>12</sub> (B) The atomic structure of FeNi<sub>3</sub>

The calculation uses the LSDA approximation to find ground state lattice constants by optimizing structure parameters. The Birch-Murnaghan's equation of state follows as the next step.

$$E(V) = E_0 + \frac{9V_0 B_0}{16} \left\{ \left[ \left( \frac{V_0}{V} \right)^{2/3} - 1 \right]^3 B'_0 + \left[ \left( \frac{V_0}{V} \right)^{2/3} - 1 \right]^2 \left[ 6 - 4 \left( \frac{V_0}{V} \right)^{2/3} \right] \right\}$$
(3.1)

V<sub>0</sub> represents the volume while B<sub>0</sub> stands for bulk modulus and E<sub>0</sub> represents the total ground state energy during the analysis process. Total energy serves to evaluate both the internal system components and the convergence behavior of the system. We execute volume optimization for the non-magnetic as well as the ferromagnetic and antiferromagnetic states after setting their configurations. Fig. (3.2) presents volume optimization data which demonstrates that DyFe<sub>3</sub>Ni<sub>12</sub> possesses ferromagnetic characteristics because ferromagnetic state resulted in the minimum total energy relative to other magnetic states. The final energy analysis shows that DyFe<sub>3</sub>Ni<sub>12</sub> has the most stable state when it exists in a ferromagnetic arrangement.



**Figure 3.2:** Volume optimization curve shows the 3 states (Antiferromagnetic Green line, Ferromagnetic Red line and non-magnetic blue line).

The next step requires evaluation of structural parameters including lattice parameter (a) and minimal volume (V) regarding cohesive energy ( $E_{coh}$ ) [7] and formation energy ( $\Delta E_{form}$ ) [8] separately. Table (3.2) presents structural data which provides information about the material's stability features alongside its bonding characteristics. The optimized crystal structure exhibits the lattice parameter whereas minimal volume represents material stability. The cohesive energy defines material bonding strength and formation energy indicates material resistance to its constituent elements.

Compound	Lattice parameter (a)	Volume	ECoh	ΔEform	В'	Young module B
DyFe <sub>3</sub> Ni <sub>12</sub>	<b>6.999</b> Å	342.853 Å <sup>3</sup>	164.52 eV	-1.444 eV	4.8662 GPa	222.4305 GPa
FeNi <sub>3</sub> [26]	3.537 Å	$44.264 \text{ Å}^3$	/	-0.090 eV	/	199 GPa

**Table 3.2:** The structural result after getting minimal energy by using Birch-Murnaghan's equation.

#### 3.4 Magnetic results:

Table (3.3) below shows the calculated magnetic moment and per atom moment after confirming ferromagnetic behavior of DyFe<sub>3</sub>Ni<sub>12</sub> From the minimal energies.

Compound	Moment per atom $(\mu_B)$	Moment total $(\mu_B)$	
DyFe3Ni12	Dy= 4.89636 Fe= 2.78965 Ni= 0.49715	18.96928	
FeNi3 [27]	/	5.28	

Table 3.3: Magnetic data of the intermetallic DyFe<sub>3</sub>Ni<sub>12</sub> and FeNi<sub>3</sub>

In the magnetic moments per atom calculations of DyFe<sub>3</sub>Ni<sub>12</sub> some combination of elements emerges where Dy rare earth atom reveals a significant value of nearly 4.90  $\mu_B$ . High atomic magnetic moment appears in Dysprosium chemistry because its 4f electrons create stable localized magnetic moments through minimal neighbor interactions.

The magnetic property of Fe atoms amounts to  $2.79~\mu_B$  highlighting their ferromagnetic alignment as present in transitional metals that feature partially filled 3d orbitals. The strengthened magnetism within the Fe sub-lattice makes these active Fe atoms likely to enhance material magnetic properties because of this high magnetic moment value.

The incorporation of Nickel (Ni) atoms in DyFe<sub>3</sub>Ni<sub>12</sub> material produces magnetic moments ranging at  $0.50~\mu_B$  without affecting the magnetism levels in this system. The magnetic arrangement of Ni atoms occurs through Fe atomic interactions together with the prospect of Dy atomic interactions since Ni atoms do not become overly magnetic in this system.

Based on our calculations the DyFe<sub>3</sub>Ni<sub>12</sub> has a total magnetic moment of 18.97  $\mu_B$  for each formula unit proving its significant magnetic properties. The significant total magnetic moment of DyFe<sub>3</sub>Ni<sub>12</sub> underlines the combined magnetic properties of all Dy, Fe and Ni atoms thus enabling the material to operate as a promising magnetic technology requiring high magnetic moments.

#### 3.5 Electronic structures:

# 3.5.1 Partial density of states:

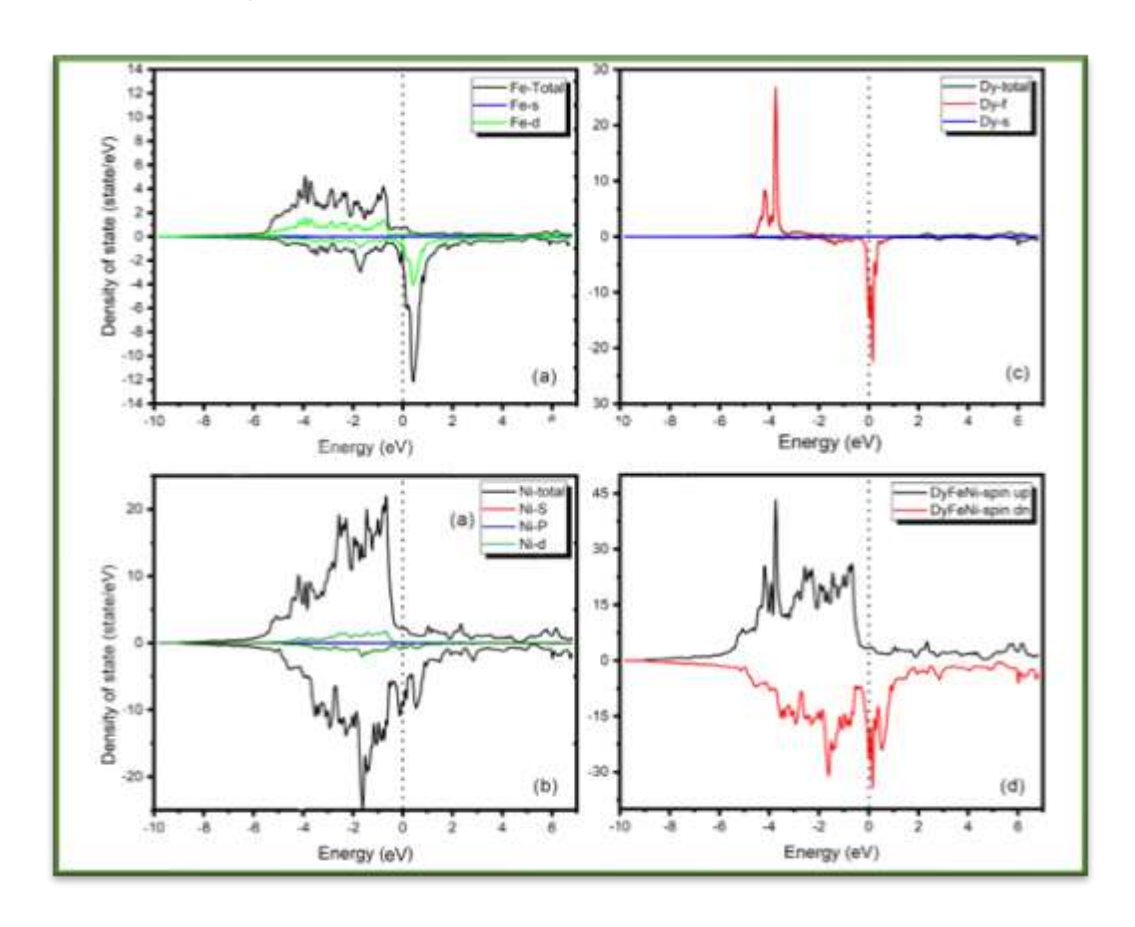


**Figure 3.3:** Shows the curves of density of state of DyFe3Ni12, (a) represent the iron-Fe curve, (b) illustrate the Nickel-Ni curve, (c) show the Dysprosium-Dy curve and (d) the total dos of DyFe3Ni12

Fig. (3.3.a) Displays the density of states for Iron (Fe) which serves as a technological metal mainly because of its ferromagnetic behavior. This graph illustrates both the total DOS and its component parts from s-orbitals and d-orbitals. For the energy values the Fermi level defines the reference point where the value equals zero. The result establishes that d-orbital electronic states clearly dominate the states near the Fermi level by showing distinct peaks in the green curve. D-electrons dominate the electronic properties of transition metal such as Fe which leads to significant effects in its magnetic and electronic behavior. The localized states present in the DOS data at -4 eV have a dominant influence on the ferromagnetic properties of the material due to their distinct features. The study confirms the Stoner model prediction of spontaneous magnetization at positions where the Fermi level contains high density of states [9]. The s-orbital states show negligible participant in essential electronic interactions near the Fermi energy level as exemplified by the blue curve. The DOS profile highlights the dominant role of d-electrons in both magnetic properties and conduction nature of iron while certifying it as a fundamental d-band metal.

The Density of States plot depicted in Fig. (3.3.b) demonstrates the orbital components from s, p and d groups of Nickel (Ni). This diagram sets the Fermi level at 0 electron Volt while using electron Volt units as its measurement standard. The entire DOS exhibits an extensive black-colored peak near the Fermi level that results from d-orbital states indicated in green. Nickel demonstrates dominant d-electron behavior which determines its high electrical conductance and magnetic capabilities because of its electronic structure [10]. According to d-band theory the positioning of the d-band center affects catalytic activity hence explaining why d-electrons play a vital role in electronic and catalytic applications [11]. Near the Fermi level, s and p orbitals have an extremely low contribution according to the red and blue curves displayed in the results. Experimental data shows that d-electrons represent the dominant component for producing fundamental properties of both catalytic activity and magnetism in nickel metal. The d-bands in DOS show narrow distributions through their pronounced definitions. Narrow bands exhibit strong electronic correlations together with potential spin-polarization effects which are essential for spintronic applications.

The DOS distribution of Dysprosium (Dy) appears in Fig. (3.3.c) where the calculation shows separate DOS measurements of both spin-up and spin-down states. The black line depicts Dy-total which integrates the entire DOS structure of Dysprosium through its spin-up and spin-

down states while the curve symmetry below and above the x-axis measures the balance of its spin states. There are multiple discernible features in Dysprosium's total density of states curves that stem directly from its strong spin-dependence characteristic found in magnetic materials. The red line (Dy-f) indicates sharp peaks which appear in the red curve below the Fermi level at -4 eV suggesting that f electrons mainly determine magnetic properties. Dysprosium reveals extensive f electron dominance in its magnetic system because of significant variations between spin-up and spin-down contributions at these peaks. The self-symmetrical s electron contribution exists to a small extent for both the spin up and spin down states of Dy-s orbitals. The weak nature of s electron delocalization prevents them from affecting material magnetic responses therefore their influence remains weak based on these data. The analysis depicts some distribution of state (DOS) for Dysprosium where spin up and spin down DOS exhibit noticeable differences particularly in areas containing f electron states. The significant difference between spin up and spin down states establishes the magnetic property of Dysprosium. The strong spin polarization of f electrons beneath the Fermi level proves beyond doubt that they determine Dysprosium's magnetic properties. Sharp f spin polarized DOS peaks demonstrate the localized strong nature of magnetic f interactions.

#### **3.5.2 Total DOS:**

Fig (3.3.d) shows the spin polarization of the DyF<sub>3</sub>Ni<sub>12</sub> obtained through compound DOS analysis which delivers essential details about the electrical and magnetic characteristics. The DOS analysis separates electron states for both the spin-up and spin-down electrons which indicates the material contains substantial magnetic ordering. DOS shows strong peaks just below the Fermi level which specifically locate at -4 eV because of localized electronic states from Dy and f and Fe and Ni. The asymmetric distribution of spin-up and spin-down states also features below the Fermi energy indicating this material has an inherent magnetic moment that can demonstrate ferromagnetic or ferrimagnetic behavior in DyFe<sub>3</sub>Ni<sub>12</sub>. The DOS imbalance that occurs at the Fermi level specifically indicates that spin-dependent interactions exist in this material to create its magnetic properties. The electronic states that localize at -4 eV indicate a robust magnetic bond between atomic elements which establishes f-electron contributions from Dysprosium while delectron contributions mainly come from Nickel and Iron. Spin-polarized DOS shows that

electronic structure stands as a crucial factor to explain DyFe<sub>3</sub>Ni<sub>12</sub>'s magnetic behavior which means it has potential as a significant subject for spintronic and magnetic material research.

### 3.5.3 BAND STRUCTURE:

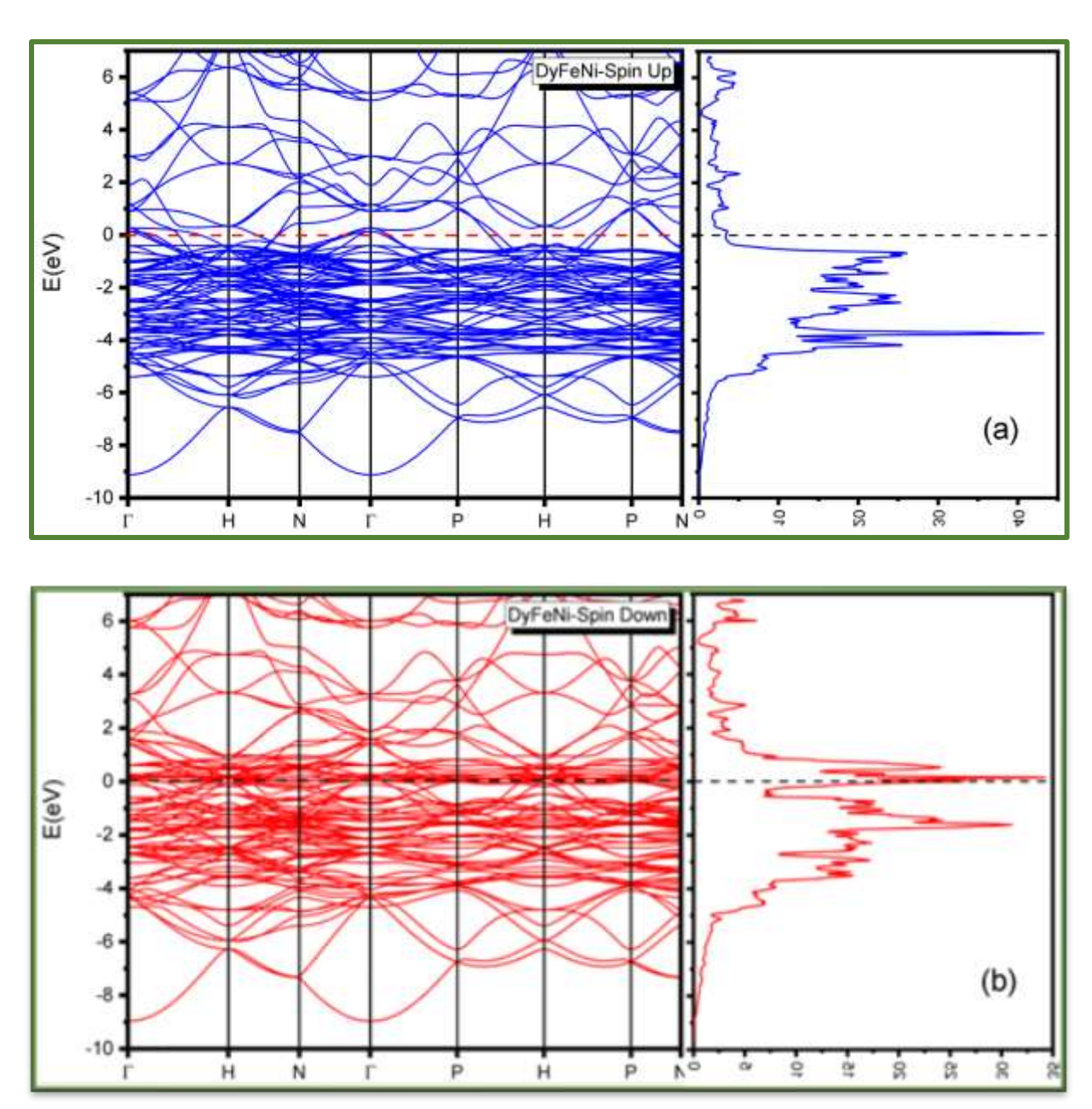


**Figure 3.4:** The band structure of DyFe<sub>3</sub>Ni<sub>12</sub> with (a) represent spin up bands and the (b) show the spin down bands and the both attached with dos curves.

The Brillouin zone depiction of the spin-up channel follows the high symmetry points Γ, H, N and P for DyFe<sub>3</sub>Ni<sub>12</sub>. as shown in Fig. (3.4.a). The majority spin structure contains bands that intersect the Fermi level which confirms its metallic nature in each spin channel. Both spin-up and spin-down band structures need closer analysis to detect any asymmetry patterns that would indicate spin-polarized characteristics. This material shows band asymmetries which indicate its potential use as a spin-dependent transport system for spintronics applications together with DyFe<sub>3</sub>Ni<sub>12</sub> [12]. The spin-dependent band structures properly explain DyFe<sub>3</sub>Ni<sub>12</sub> magnetic properties which makes it highly promising for possible strong magneto-resistance effects during spintronics device development.

This work featured Fig. (3.4.b) showing the DyFe<sub>3</sub>Ni<sub>12</sub> electronic band structure spin-down signal which moved identically through the Brillouin zone with the spin-up data l. Some electronic bands from the Fermi level indicate metallic behavior in the spin down channel of the system. Electron conductance in the spin-down state mainly arises from the crossing patterns observed between electronic bands. In transition metal-based alloys such nature appears because the d band states possess numerous states that allow a high states density at Fermi level resulting from band overlap [13]. Numerous crossing bands in the band structure reveal significant d-state and f-state interactions and hybridization between Fe and Ni atoms and between Dy components. The magnetic characteristic variations and spin polarization potential make this material suitable for both magnetic storage and spintronic applications [14]. DyFe<sub>3</sub>Ni<sub>12</sub> demonstrates excellent spindown electron conductivity because the material lacks a band gap.

## 3.6 Elastic properties:

A set of characteristics are defined through elastic moduli like young's modulus, shear modulus, and others, as well as elastic wave velocities (compressional and shear) [15]. These properties provide light on the material's ability to withstand external loads, as well as the specific threshold values at which it can maintain mechanical strength [16]. In order to obtain mechanical properties, the  $C_{ij}$  parameters must be determined, they are, respectively ( $C_{11}$ ,  $C_{12}$ ,  $C_{44}$ ) [17], predictions of longitudinal compression, transverse expansion, and shear modulus. Moreover, the factors are explicit of Im-3m space group, a cubic crystal should undergo the Born and Huang conditions [18] to be mechanically stable. which encompass three specific criteria:

$$\begin{cases} C_{11} + 2C_{12} > 0 \\ C_{11} - C_{12} > 0 \\ C_{11} > 0, C_{44} > 0 \end{cases}$$
(3.2)

We using the DFT Method to get elastic proprieties developed by Morteza Jamal IRelast package [19], Using the elastic constants presented in Table 4, many properties will be calculated including, Young's modulus (E), anisotropy factor (A), Pugh's ratio (B/G), Voigt- Reuss shear modulus (G), Cauchy pressure (CP), Poisson's ratios (v), bulk modulus.

The bulk modulus (B) measures a substance's resistance to compressive forces. Defined as:

$$B = \frac{B_V + B_R}{2} \tag{3.3}$$

Where 
$$B_V = \frac{C_{11} + 3C_{12}}{3}$$
 (3.4)

and 
$$B_R = \frac{c_{11} + 3c_{12}}{3}$$
 (3.5)

Reuss and Voigt [20] can formulate the bulk (shear) modulus developed as  $B_R(G_R)$ , and  $B_V(G_V)$  respectively. The information of the hardness of material can be provided by shear modules and the value of intrinsic rigidity of materials can be calculated by the young's modulus using the following equation

$$G = \frac{G_V + G_R}{2} \tag{3.6}$$

Where 
$$G_V = \frac{c_{11} - c_{12} + 3c_{44}}{5}$$
 (3.7)

And 
$$G_R = \frac{(C_{11} - C_{12})5C_{44}}{4C_{44} + 3(C_{11} - C_{12})}$$
 (3.8)

Measuring the stiffness of a solid material is Young's Modulus (Y), which is also known as the modulus of elasticity. It measures the degree of stretching or compression a material will undergo in response to a given force.

$$Y = \frac{9GB}{G + 3B} \tag{3.9}$$

In physics, anisotropy denotes the directional dependence of characteristics in a crystal. The Zener anisotropy factor (A) serves to quantify both the extent of anisotropy and the presence of microcracks. Motioned in Equation (10)

$$A = \frac{2C_{44}}{C_{11} - C_{12}} \tag{3.10}$$

In materials demonstrating isotropy, the value of 'A' must precisely be 1. Any deviation from this value would indicate that the material is anisotropic [21]. The brittleness or ductility of DyFe<sub>3</sub>Ni<sub>12</sub> [22] can be deduced from Pugh's ratio B/G.

The ductility of a material can be determined by the following conditions:

$$\frac{B}{G} > 1.75$$
 for ductile materials (3.11)

$$\frac{B}{G} < 1.75$$
 for brittle materials (3.12)

Investigated Pugh's ratio values presented in Table 3 also establish the ductile characteristics of DyFe<sub>3</sub>Ni<sub>12</sub>.

The structural stability of a material can be determined from its internal deformation coefficient ( $\xi$ ). The values of  $\xi$  for DyFe3Ni12 are shown in Table 4. The estimated elastic constants (C11 and C12) are used to solve for  $\xi$  by Equation (13).

$$\xi = \frac{c_{11} + 8c_{12}}{7c_{11} - c_{12}} \tag{3.13}$$

The Poisson ratio v, which assesses a material's capacity to compress, is mathematically represented as follows:

$$\nu = \frac{3B - 2G}{2(3B + G)} \tag{3.14}$$

 $\upsilon$  < 2.6 for brittle materials or  $\upsilon$  > 2.6 for ductile materials

Equation (15) uses the computed elastic constant  $C_{11}$  to get the melting point  $T_{mel}$ . Table (3.4) shows the  $T_{mel}$ :

$$Tmel = [553^{\circ}K + (5.19 \times C_{11})] \pm 300^{\circ}K$$
 (3.15)

	DyFe <sub>3</sub> Ni <sub>12</sub>	FeNi <sub>3</sub>
Elastic parameters	Values	Values
$C_{II}$	309 GPa	285 GPa
$C_{12}$	179 GPa	156 GPa
C <sub>44</sub>	132 GPa	134 GPa
В	222 GPa	199 GPa
$G_R$	93 GPa	94 GPa
$G_{v}$	105 GPa	106 GPa
G	99 GPa	100 GPa
Y	260 GPa	257 GPa
Poisson's Ratio (v)	0.3055	0.29
Pugh's Ratio (B/G)	2.2377	1.99
Frantesvich's Ratio (G/B)	0.4469	0.50
Anisotropy (A)	2.0444	0.67
Internal Strain (ζ)	0.8791	
Melting Temperature $(T_{mel})$	$2378 \pm 300 \text{ K}$	1438 K

Table 3.4: Values of elastic proprieties of DyFe<sub>3</sub>Ni<sub>12</sub> and FeNi<sub>3</sub>

Computed elastic properties of DyFe<sub>3</sub>Ni<sub>12</sub> from table (3.4) provide important information on mechanical stability with good practical applicability. Specifically, the three major elastic constants,  $C_{11}$ ,  $C_{12}$ , and  $C_{44}$ , are determined to be 309 GPa, 179 GPa, and 132 GPa, respectively, reflecting strong interatomic forces with a firm structural background. Also, with a bulk modulus B = 222 GPa under applied pressure, the resistance to volume compression is very high. The

theoretical shear moduli of  $G_R = 93$  GPa,  $G_v = 105$  GPa, and the average G= 99 GPa indicate fair resistance to the shape deformation that enhances the rigidity of the compound as a whole. The attained value of the Young's modulus Y=260 GPa gives evidence for important stiffness whereas the Poisson's ratio is equivalent to 0.3055, showing quite good stability with some brittleness.

Pugh ductility to brittleness is 2.24, hence balanced, Frantesvich's ratio is 0.45 and elastic anisotropy factor A is 2.04, thereby indicating that the material is anisotropic elastically and hence would show mechanical response variance with crystallographic direction. The internal strain,  $\xi$  has been computed to be 0.8791 within the generally observed range and representing minimum distortion under the applied stress. Besides, the calculated melting temperature of 2378  $\pm$  300 K reflects high thermal resistance and further indicates that DyFe<sub>3</sub>Ni<sub>12</sub> can be used under high-temperature conditions. The characteristics all combined support DyFe<sub>3</sub>Ni<sub>12</sub> for application in conditions requiring resistance against mechanical failure and thermal stability.

#### 3.7 Thermoelectric result:

Using the Boltzmann transport theory, the BoltzTrap code allows us to calculate thermoelectric properties. To exhibit promising thermoelectric properties, the electrical conductivity is high, the Seebeck coefficient is large and the electronic thermal conductivity is as low as possible. A high electrical conductivity enables good charge carrier movement within the material, while a large Seebeck coefficient manifests the potential of a material for converting temperature difference into electric voltage. The low electronic thermal conductivity is similarly important because it restricts heat transfer through the charge carriers, thereby maintaining the temperature gradient necessary in devices for appropriate thermoelectric performance [23].

We theoretically studied the thermoelectric properties in the 50-800 K temperature range by considering the main relevant parameters, by way of electrical conductivity  $\sigma/\tau$ , with  $\tau$  as the relaxation time, Seebeck coefficient S, electronic thermal conductivity  $\kappa^0/\tau$ , power factor  $S^2\sigma$ , and figure of merit ZT. All the properties plotted in this temperature range are for a fixed chemical potential, i.e.,  $\mu$ =EF= 0.69205 Ry., where EF is the Fermi energy. This amount of chemical potential offers the opportunity to regularly compare and estimate thermoelectric efficiency for various temperatures.

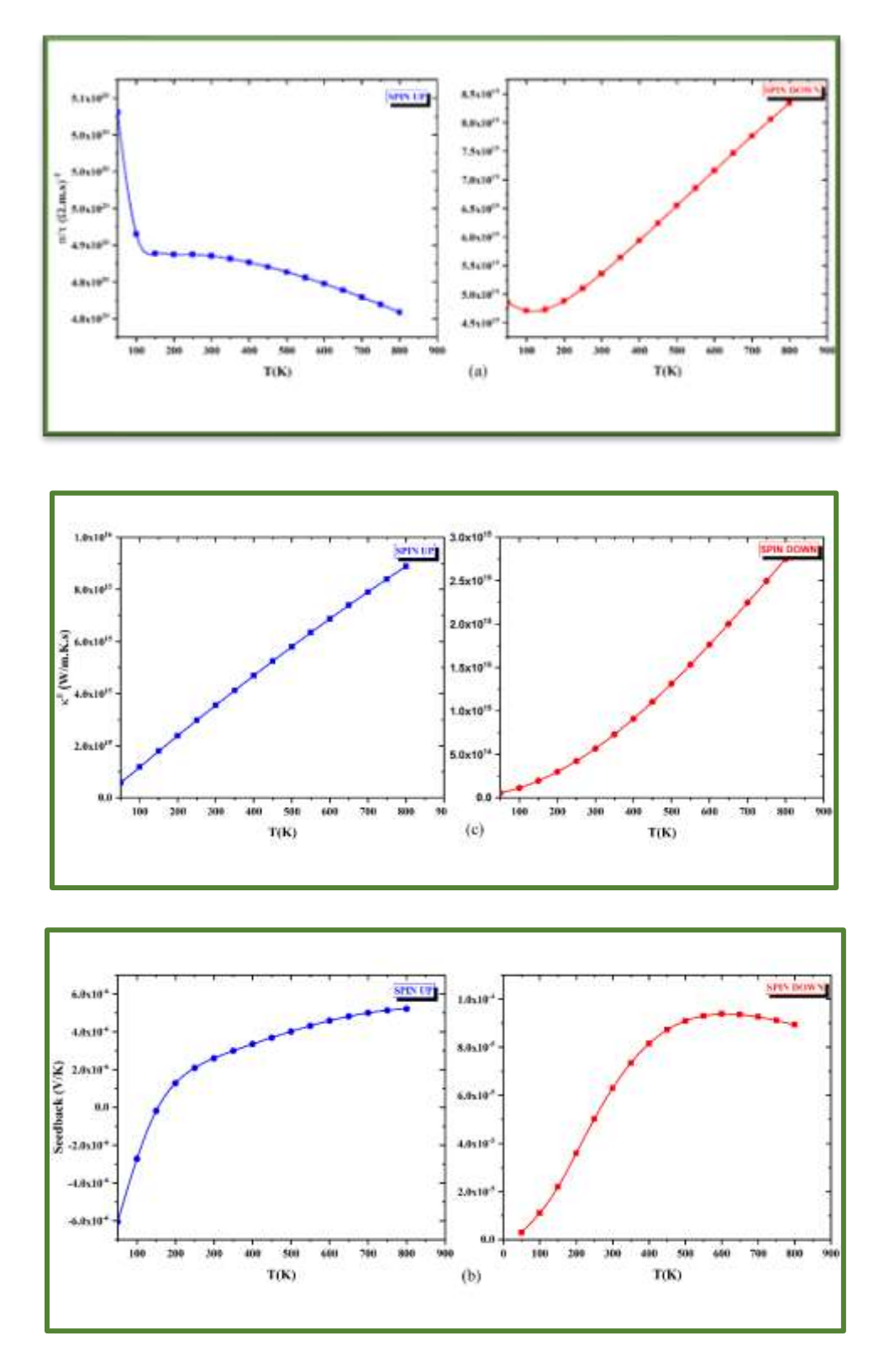


Figure 3.5: The conductivity the electrical  $\sigma$  (a) and Seebeck coefficient S (b), thermal conductivity  $\kappa 0$  (c) curves.

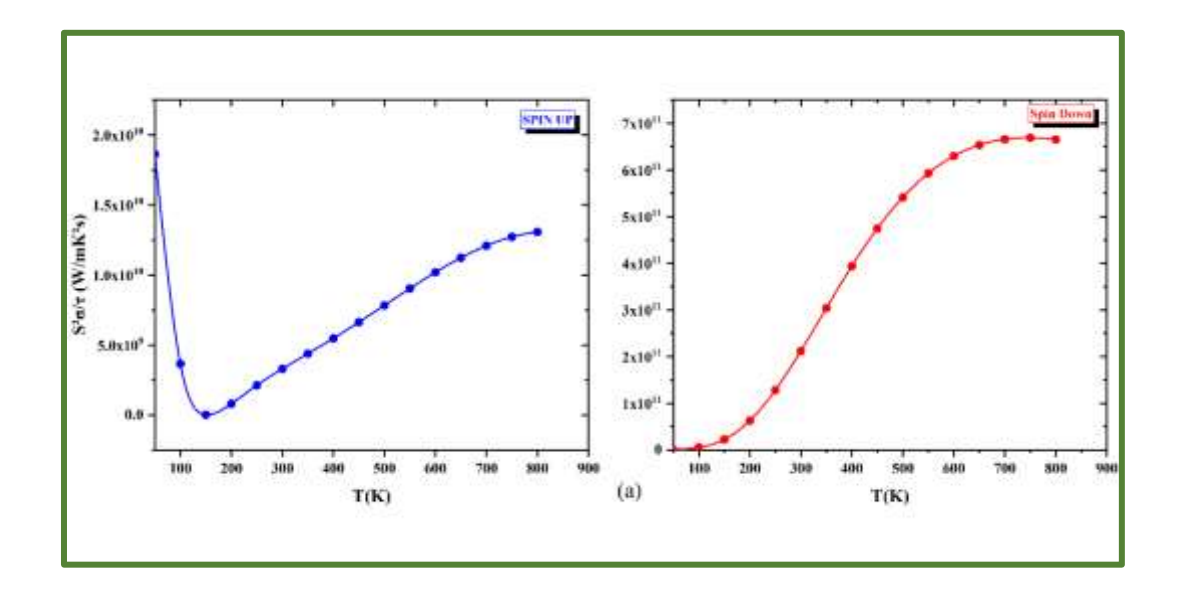
Fig. (3.5.a) illustrates the temperature dependency of the electrical conductivity each value of relaxation time  $\sigma/\tau$ , for the spin-up and spin-down states of the intermetallic compound DyFe<sub>3</sub> Ni<sub>12</sub> the  $\sigma$  values for the spin-up part initially exhibit a high conductivity value of approximately  $5.1\times10^{20}\,(\Omega\cdot\text{m}\cdot\text{s})^{-1}$  at low temperatures, which rapidly decreases as temperature increases up to around 100 K. Beyond this point, the conductivity stabilizes, with a slow decline observed across the higher temperature range, reaching a value around  $4.8\times10^{20}\,(\Omega\cdot\text{m}\cdot\text{s})^{-1}$  at 800K. This curve suggests that the spin-up carriers in DyFe<sub>3</sub>Ni<sub>12</sub> have high mobility at low temperatures, but as temperature rises, thermal scattering likely reduces their effective conductivity, leading to a relatively stable but diminished  $\sigma/\tau$  at higher temperatures.

for the spin-down component, which display a distinctly different temperature dependence. The conductivity starts off low at about  $4.5 \times 10^{19} \, (\Omega \cdot m \cdot s)^{-1}$ , and almost begins to rise in a straight line upon increasing temperature and 800 K where it levels off at around  $8.5 \times 10^{19} \, (\Omega \cdot m \cdot s)^{-1}$ . This indicates, that the presence of heat is probably aiding the mobility or concentration of carrier spins of DyFe<sub>3</sub>Ni<sub>12</sub> that are usually referred to as spin down, which works against the normally scattering effect [24] which reduces conductivity with temperature rise. It might be an indication of peculiar features in the electronic band structure with respect to the spin down state for this solid. Across the spin down and spin up channels, the spin dependent electrical properties of DyFe<sub>3</sub>Ni<sub>12</sub> are shown by lower  $\sigma/\tau$  ratio where the  $\tau$  is the relaxation time. There is spin up channel conductivity suppression with temperature rise which is likely associated with increased phonon or defect scattering, however, the spin down channel has findings of thermal enhancement in conductivity which suggests that the carrier dynamics might enhance from the action of heat. Due to this opposing behavior, DyFe<sub>3</sub>Ni<sub>12</sub> is suitable for spintronic or thermoelectric applications where the spin-polarized conductivity needs to be controlled.

The spin-up component of the Seebeck coefficient displayed in Fig. (3.5.b) shows a negative S value of about  $-6.0 \times 10^{-6}$  V/K at low temperature which corresponds to carrier conduction of electrons. With increase in temperature, although the S value remains negative, it gradually tends to become positive with the zero cross over happening at about 150 K. After this temperature, the coefficient rises more suspect and reaches a maximum value of about  $+4.0 \times 10^{-6}$  V/K at high temperatures where it appears to level off. This behavior signifies that with increased temperatures, there is a transition in thermoelectric conduction from electron like (negative S)

conduction to hole like (positive S) conduction due, the movement of carriers with temperature is believed to cause a change in the electronic band structure. In the case of the spin down branch, the Seebeck coefficient is seen to vary positively in the whole range of temperatures, very close to zero at first and quite rapidly increasing to approximately  $8.0 \times 10^{-5}$  V/K at around 300 K. Above this temperature, the coefficient continues to increase, although at a gentler rate, increasing up to a certain value and then ceasing to change. The spin down channel has a significantly larger positive Seebeck coefficient which infers that hole-like conduction could be active. The observation that the Seebeck coefficients related with the spin up and spin down components of the thermoelectric material vary considerably suggests the presence of a significant spin thermoelectric effect which is likely beneficial in relation to its bearing on materials suitable for spintronics [25] and designed thermoelectric materials.

In Fig. (3.5.c), the thermal conductivity coefficients  $\kappa 0$  of DyFe<sub>3</sub>Ni<sub>12</sub> in both spin orientations display a close to linear increase in thermal conductivity with temperature. Whereas with regard to the up-spin channel, the value of  $\kappa 0$  reaches 9 x10<sup>15</sup> W/m.K.s at a temperature of 800K, the down spin channel value is 2.75 x10<sup>15</sup> on the same spin up channel. This linear growth indicates that thermal conductivity is a function of temperature in the sense that it is less at low thermal energy but increases with increase in thermal energy. It appears that the thermal conductivity of DyFe<sub>3</sub>Ni<sub>12</sub> is largely influenced by the spin-up channel especially for higher temperatures. The notable disparity in conductivities with respect to spin up and down states could lead to interesting uses in turn on and turn off thermal and electrical conductance in devices like thermoelectric and spintronic devices, which would take advantage of heat and electrical flow based on spins.



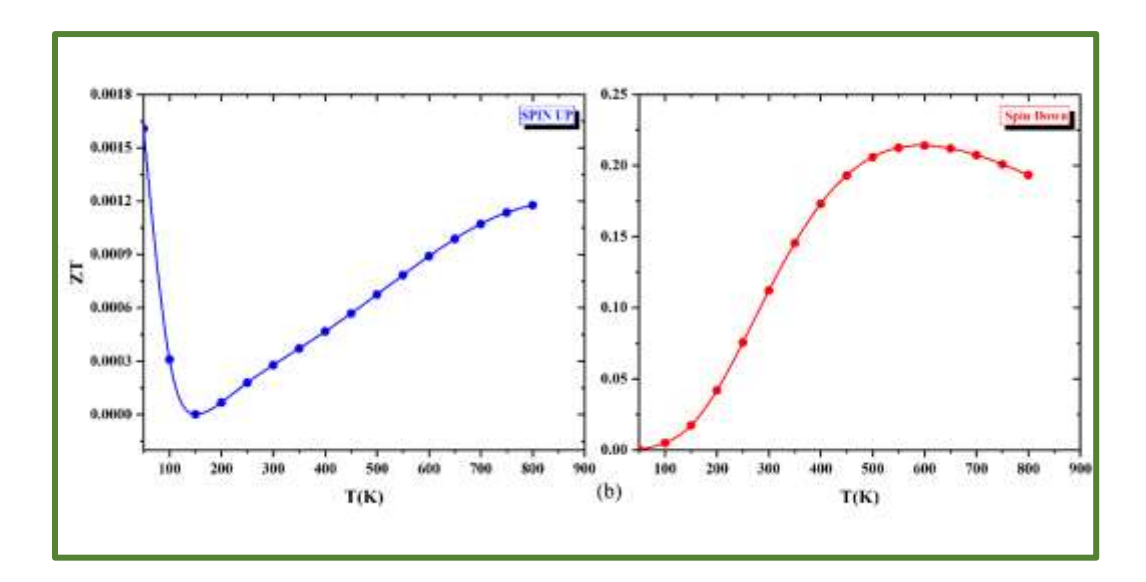


**Figure 3.6:** The curves of Power factor PF (a) and figure of merit ZT (b) with both spins (spin up with blue color and spin down with red color).

Fig. (3.6.a) Shows the change in power factor with increasing spin up and increasing spin down in a DyFe<sub>3</sub>N<sub>12</sub>, the power factor for the spin up begins with a value of  $1.8 \times 10^{10} \text{ W/m.K}^2$ .s at 50K there is an explosive drop to zero at 150K, further to that the PF Value begin to rise with elevation of the temperature until a value of a  $1.25 \times 10^{10} \text{ W/m.K}^2$ .s is attained at 800K temperature. The PF for the spin-down channel shows a different trend, where it begins almost at zero value and rises with temperature until it attains a maximum value of  $6.5 \times 10^{11}$  at about 700 K, and

thereafter maintains stable values at higher temperatures. This indicates that the spin-down channel might benefit the thermoelectric enhancement only at high temperatures regions.

In general, DyFe<sub>3</sub>Ni<sub>12</sub> demonstrates opposite trends with respect to the spin-up and the spin-down channels, and these features may be used in spintronic devices in which the transport of one of the spins is sought. Both channels exhibit high PF at higher temperatures, hence DyFe<sub>3</sub>Ni<sub>12</sub> may have potential use in thermoelectric applications operating at elevated temperatures.

As it can be realized in fig. (3.6.b), irrespective with the spin orientation, the figure of merit (ZT) remains low. To be more specific, the spin up component has a ZT value of 0.0016 at 50 K and begins to decrease to 0 as high as 150 K. And after that, between 150 K and 800 K, ZT gets a bit higher than before and reaches a value of 0.0012. All these changes indicate that there is poor or low thermoelectric performance in the given range of temperature, and little or no variation in the performance is attained above 150 K.

On the other hand, the spin-down component has been shown to climb in its figure of merit (ZT) from zero and even up to a highest ZT value of 0.22 at operating temperatures ranging from 100 K to 600 K. This ZT reaches a peak and after that, there is a drop unit ZT = 0.20 observed between 600 K and 800 K. This higher value and the subsequent lower value imply that the contribution of spin down plays an important role in attaining high thermoelectric performance up to 600 K, but loses some effectiveness for higher temperature

### **References:**

- [1] Gignoux, D., & Schmitt, D. (1991). Rare earth intermetallics. Journal of Magnetism and Magnetic Materials, 100(1–3), 99–125. https://doi.org/10.1016/0304-8853(91)90815-r.
- [2] Buschow, K. H. J., & De Boer, F. R. (2003). Permanent Magnets. In *Springer eBooks* (pp. 105–129). <a href="https://doi.org/10.1007/0-306-48408-0\_12">https://doi.org/10.1007/0-306-48408-0\_12</a>.
- [3] Anisimov, V. I., et al. "Density-functional Theory and NiO Photoemission Spectra." Physical Review. B, Condensed Matter, vol. 48, no. 23, Dec. 1993, pp. 16929–34. <a href="https://doi.org/10.1103/physrevb.48.16929">https://doi.org/10.1103/physrevb.48.16929</a>.
- [4] Von Barth, U., and L. Hedin. "A Local Exchange-correlation Potential for the Spin Polarized Case. I." Journal of Physics C Solid State Physics, vol. 5, no. 13, July 1972, pp. 1629–42. https://doi.org/10.1088/0022-3719/5/13/012.
- [5] Birch, Francis. "Finite Elastic Strain of Cubic Crystals." Physical Review, vol. 71, no. 11, American Physical Society (APS), June 1947, pp. 809–24. Crossref, <a href="https://doi.org/10.1103/physrev.71.809">https://doi.org/10.1103/physrev.71.809</a>.
- [6] Bac, L., Kwon, Y., Kim, J., Lee, Y., Lee, D., & Kim, J. (2009). Synthesis and characteristic of FeNi3 intermetallic compound obtained by electrical explosion of wire. *Materials Research Bulletin*, 45(3), 352–354. <a href="https://doi.org/10.1016/j.materresbull.2009.12.008">https://doi.org/10.1016/j.materresbull.2009.12.008</a>.
- [7] Srivastava, G. P., & Weaire, D. (1987). The theory of the cohesive energies of solids. *Advances in Physics*, *36*(4), 463–517. <a href="https://doi.org/10.1080/00018738700101042">https://doi.org/10.1080/00018738700101042</a>.
- [8] Tzanetakis, P., Hillairet, J. and Revel, G. (1976), The Formation Energy of Vacancies in Aluminum and Magnesium. phys. stat. sol. (b), 75: 433 https://doi.org/10.1002/pssb.2220750205.
- [9] Kübler, Jürgen. "Theory of Itinerant Electron Magnetism, 2nd Edition." *Oxford University Press eBooks*, 2021, <a href="https://doi.org/10.1093/oso/9780192895639.001.0001">https://doi.org/10.1093/oso/9780192895639.001.0001</a>.
- [10] Singh, David J. "Planewaves, Pseudopotentials and the LAPW Method." Springer eBooks, 2006, <a href="https://doi.org/10.1007/978-0-387-29684-5">https://doi.org/10.1007/978-0-387-29684-5</a>.

- [11] Nørskov, Jens K., et al. "Density Functional Theory in Surface Chemistry and Catalysis." Proceedings of the National Academy of Sciences, vol. 108, no. 3, Jan. 2011, pp. 937–43. <a href="https://doi.org/10.1073/pnas.1006652108">https://doi.org/10.1073/pnas.1006652108</a>.
- [12] Miyazaki, T., and N. Tezuka. "Giant Magnetic Tunneling Effect in Fe/Al2O3/Fe Junction." *Journal of Magnetism and Magnetic Materials*, vol. 139, no. 3, Jan. 1995, pp. L231–34. <a href="https://doi.org/10.1016/0304-8853(95)90001-2">https://doi.org/10.1016/0304-8853(95)90001-2</a>.
- [13] Planes, Antoni, et al. "Magnetocaloric Effect and Its Relation to Shape-memory Properties in Ferromagnetic Heusler Alloys." *Journal of Physics Condensed Matter*, vol. 21, no. 23, May 2009, p. 233201. https://doi.org/10.1088/0953-8984/21/23/233201.
- [14] Keshavarz Hedayati, Samara. "Magnetism in Transition Metal Systems: Interplay Between Structure, Dimensionality and Electron Correlation." *Digital Comprehensive Summaries of Uppsala Dissertations from the Faculty of Science and Technology*, vol. 1720, Acta Universitatis Upsaliensis, 2018, www.diva-portal.org/smash/get/diva2:1241591/FULLTEXT01.pdf.
- [15] Schön, Jürgen H. "Elastic Properties." *Developments in Petroleum Science*, vol. 167–268, 1 Jan. 2015, https://doi.org/10.1016/b978-0-08-100404-3.00006-8.
- [16] Abbas, Zeesham, Zeeshan Zafar, et al. "Density-functional Quantum Analysis of Optoelectronic, Elastic, Thermodynamic and Hydrogen Storage Properties of AMgH3 (a= Be, Ca) Perovskite-type Hydrides: Prospects for Clean Energy Hydrogen-storage Fuel and Optoelectronic Applications." *International Journal of Hydrogen Energy*, vol. 60, Feb. 2024, pp. 212–28. <a href="https://doi.org/10.1016/j.ijhydene.2024.02.081">https://doi.org/10.1016/j.ijhydene.2024.02.081</a>.
- [17] Kumari, Preeti, et al. "DFT Calculations of Opto-electronic, Mechanical, Thermodynamic, and Transport Properties of XCeO3 (X = Mg, Ca, and Ba) Perovskite." *The Journal of Chemical Thermodynamics*, vol. 184, May 2023, p. 107071. https://doi.org/10.1016/j.jct.2023.107071.
- [18] Born, Max, and Kun Huang. *Dynamical Theory of Crystal Lattices*. 1996, https://doi.org/10.1093/oso/9780192670083.001.0001.
- [19] Jamal, M., et al. "IRelast Package." *Journal of Alloys and Compounds*, vol. 735, Nov. 2017, pp. 569–79. <a href="https://doi.org/10.1016/j.jallcom.2017.10.139">https://doi.org/10.1016/j.jallcom.2017.10.139</a>.

- [20] Voigt, W. "Ueber Die Beziehung Zwischen Den Beiden Elasticitätsconstanten Isotroper Körper." *Annalen Der Physik*, vol. 274, no. 12, Jan. 1889, pp. 573–87. <a href="https://doi.org/10.1002/andp.18892741206">https://doi.org/10.1002/andp.18892741206</a>.
- [21] Abbas, Zeesham, Kisa Fatima, et al. "A DFT+U Study of the Effect of Transition Metal Replacements on Optoelectronic and Elastic Properties of TmCu3S4 (Tm = V, Ta, Nb)." *Optik*, vol. 250, Nov. 2021, p. 168289. https://doi.org/10.1016/j.ijleo.2021.168289.
- [22] Abubakr, Muhammad, et al. "Systematic Study on the Optoelectronic and Elastic Properties of Cu-based Ternary Chalcogenides: Using Ab-initio Approach." *Materials Science in Semiconductor Processing*, vol. 162, Apr. 2023, p. 107512. https://doi.org/10.1016/j.mssp.2023.107512.
- [23] M. Torrichi. (2021). Theoretical Study of Electronic and Thermoelectric Properties of Sodium Doped 4H-GaN Polytype. *Algerian Journal of Research and Technology (AJRT)*, *5*(1), 52–60. <a href="https://doi.org/10.58681/ajrt.21050106">https://doi.org/10.58681/ajrt.21050106</a>.
- [24] Wolf, S. A., et al. "Spintronics—A Retrospective and Perspective." *IBM Journal of Research and Development*, vol. 50, no. 1, Jan. 2006, pp. 101–10. <a href="https://doi.org/10.1147/rd.501.0101">https://doi.org/10.1147/rd.501.0101</a>.
- [25] Walker, C. T., and R. O. Pohl. "Phonon Scattering by Point Defects." *Physical Review*, vol. 131, no. 4, Aug. 1963, pp. 1433–42. <a href="https://doi.org/10.1103/physrev.131.1433">https://doi.org/10.1103/physrev.131.1433</a>.
- [26] Data retrieved from the Materials Project for FeNi3 (mp-1418) from database version v2025.04.10.
- [27] Horton, Matthew Kristofer, et al. "High-throughput Prediction of the Ground-state Collinear Magnetic Order of Inorganic Materials Using Density Functional Theory." Npj Computational Materials, vol. 5, no. 1, June 2019, <a href="https://doi.org/10.1038/s41524-019-0199-7">https://doi.org/10.1038/s41524-019-0199-7</a>.

# GENERAL CONCLUSION

In this thesis, we conducted a broad theoretical study of the intermetallic compound DyFe<sub>3</sub>Ni<sub>12</sub> using state-of-the-art quantum mechanical techniques based on DFT as implemented within the WIEN2k code. This work addressed an extensive range of properties, which consisted of structural, magnetic, electronic, mechanical, and thermoelectric characteristics. And we Compare it With the FeNi3 Compound which is the origin of our alloy.

The study started by giving an in-depth presentation of intermetallic alloying, including their variety of structures, formation pathways, and wide range of applications, especially in the case of rare-earth and transition metal elements. The material presented above provided a basis for interpreting the complicated features of DyFe<sub>3</sub>Ni<sub>12</sub>. The ferromagnetic state of the compound proved to be stable, as shown by the results of our structural optimization and total energy calculations. Our magnetic analysis showed a robust ferromagnetic behavior, which is mostly supported by the exchange interactions between Fe, Ni, and Dy sublattices. Studies of the electronic structure, using both density of states and band structure, showed the compound is metallic in nature, with a high spin polarization, thus confirming its magnetic state. Elastic property assessments indicated mechanical stability and ductility indicative of its ability to frame withstanding stress. Moreover, thermoelectric analysis showed moderate performance with a discernible spin dependent behavior in the transport terms implying prospective usage in spintronic and thermoelectric devices. In a nutshell, DyFe<sub>3</sub>Ni<sub>12</sub> has a compromise of useful properties that qualify it to be utilized in magnetic, structural, and energy conversion technologies. Our study does not just contribute to a better understanding of rare-earth intermetallics but also supplies a framework for future tests and materials refinements.